

# Scroll waves in isotropic excitable media : linear instabilities, bifurcations and restabilized states

Hervé Henry and Vincent Hakim

*Laboratoire de Physique Statistique\*, Ecole Normale Supérieure,  
24 rue Lhomond, 75231 Paris Cedex 05, France*  
(October 22, 2018)

Scroll waves are three-dimensional analogs of spiral waves. The linear stability spectrum of untwisted and twisted scroll waves is computed for a two-variable reaction-diffusion model of an excitable medium. Different bands of modes are seen to be unstable in different regions of parameter space. The corresponding bifurcations and bifurcated states are characterized by performing direct numerical simulations. In addition, computations of the adjoint linear stability operator eigenmodes are also performed and serve to obtain a number of matrix elements characterizing the long-wavelength deformations of scroll waves.

## I. INTRODUCTION

Depolarization waves in cardiac muscle, oxidation waves in the Belousov-Zhabotinsky (BZ) chemical medium or at the surface of certain metal catalyst and cAMP waves in colonies of slime molds are different examples of wave propagation in excitable media [1]. They can be described in similar mathematical terms although the underlying processes are of a very different nature. In a two-dimensional (2D) or quasi-two dimensional situation, the propagation of spiral waves has been observed in these three cases as well as in other excitable media [1,2]. Asides from their intrinsic scientific interest, the potential role of these remarkable waves in cardiac arrhythmias and fibrillation [3] has motivated detailed studies of their properties during the past two decades. In particular, the mechanisms of different instabilities have been intensively investigated as well as their locations determined in parameter space of simple models [4,5] and of experiments [6].

The potential relevance to cardiac dysfunction of scroll waves, the three dimensional analogs of spirals, has also been emphasized [7] but their dynamics is still less thoroughly analyzed. Visualization of the BZ reaction in 3D gels [8,9] has confirmed the existence of these complex waves. Numerical simulations have revealed that they are prone to instabilities in several parameter regimes [10–13]. In order to analyze more systematically the different possible instabilities, we report here the result of computations of the full linear stability spectrum of a straight scroll wave in a simple two-variable model of an excitable medium. This enables us to follow the different modes of deformation of a scroll wave and to investigate which type of modes become unstable in different regions of parameter space. The modes of the adjoint operator are also determined in order to compute the value of several coefficients given by matrix elements and to check proposed analytic relations. In addition, direct numerical simulations are performed to investigate the nonlinear fate of the different instabilities and to provide a detailed characterization of the restabilized bifurcated states (when they exist).

In section II, we define the studied two-variable reaction model and explain our numerical methods. Some general properties of spiral waves are also recalled. Then, we first consider in section III a straight untwisted scroll wave. It is the simplest (i.e. z-independent) extension in the third (z-) dimension of a two dimensional (xy) spiral wave. At the linear level, two possible types of instabilities are found. Modes with positive real parts can be observed on the translation bands, which correspond to z-dependent translations of the 2d spiral in the different xy-planes, or on the meander bands, which come from z-deformations of the 2d spiral meander modes. At the non linear level, the translation band instability gives rise to a scroll wave with a continuously extending core [11,12] and does not lead to a restabilized non linear state. We confirm that this type of instability is directly related [14] to the drift direction of a 2d spiral in an external field. In contrast, the meander band type of instability [15] generally restabilizes in a distorted scroll wave and no simple relation to 2d spiral drift is observed.

In section IV, we consider twisted scroll waves. A 3D steady wave is built by rotating (i.e. twisting) the 2d spiral around its rotation center as one translates it along the z-direction. We find that twist exceeding a definite

---

\*Associé au CNRS et aux Universités Paris VI et VII.

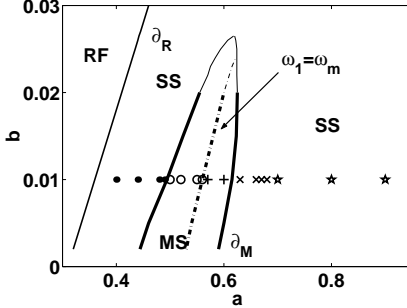


FIG. 1. Spiral bifurcation diagram for Eq. (1,2) with  $\epsilon = 0.025$  and the reaction terms of ref. [19]. The bold line  $\partial M$  is the meander threshold instability line and separates steadily rotating spirals (SS) from meandering spirals (MS) (above  $b = 0.02$  the thin line denotes our less accurate determination of  $\partial M$ ). The line  $\partial R$  marks the boundary of spiral wave existence on the left of  $\partial R$  the wave tip retracts (see e.g. ref. [14] ). The symbols along the line  $b = 0.01$  denotes the different parameters at which scroll waves are studied in the present work. Stars represent stable scroll waves, crosses ( $\times$ ) and pluses ( $+$ ) meander-unstable scroll waves, circles ( $\circ$ ), and ( $\bullet$ ) translation-band-unstable scroll waves. 2D meandering spirals are represented by (+) and ( $\circ$ ).

threshold can lead to the appearance of unstable modes in the translation bands of the scroll wave. This "sproing" [10] instability is seen to take place a finite wavevector away from the scroll wave translation symmetry mode. We provide analytical arguments which show that this very generally results from 3D rotational invariance in an isotropic medium. Nonlinear development of this instability when a single unstable mode is present results in a restabilized helical wave, as previously described [10]. Properties of these nonlinear states are computed and compared with the linear characteristics (wavevector, frequency) of the sproing instability. When several unstable modes are present in the simulation box, the scroll wave core filament takes a more complex shape which is found to travel like a nonlinear wave of constant shape in the vertical direction. Three appendices provide the details of our numerical algorithms, a derivation of a general formula for spiral drift in an external field and useful ribbon geometry formulas. A fourth one explains the relation between the present calculations and previously derived averaged equations for the motion of a weakly curved and twisted scroll wave [16,12].

The results of our linear stability analysis have previously been shortly described in [17].

## II. METHODS AND GENERAL RESULTS

### A. Reaction-diffusion model

Two-variable reaction diffusion systems have been shown to describe semi-quantitatively spiral waves dynamics and its "generic" features. They have been used in various contexts since their original introduction [18] as a simplification of Hodgkin-Huxley dynamics. The analysis of such a simple model appears in any case as a useful first step before going to a more complicated description if required. We thus follow this classic path and take for the excitable medium dynamics

$$\partial_t u = \nabla^2 u + f(u, v)/\epsilon \quad (1)$$

$$\partial_t v = g(u, v) \quad (2)$$

We only consider the singly diffusive case, the most relevant to cardiac physiology. For definiteness, we also choose reaction terms  $f(u, v) = u(1-u)[u-(v+b)/a]$ ,  $g(u, v) = u-v$  as proposed in [19]. This permits fast direct simulations and tests of our numerics by comparison with previous results for spiral waves. The 2d-spiral bifurcation diagram for this model is shown in Fig. 1 for variable values of the parameters  $a$  and  $b$  at a fixed value of  $\epsilon = 0.025$ . The meander instability line ( $\partial M$  with the notation of [5]) is plotted with its "large core" branch at smaller values of  $a$  than its "small core" branch. The crossing line which separates meander trajectories with outward petals from those with inward petals is also drawn as well as the diverging core existence boundary of spiral waves ( $\partial R$ ).

In the following, the stability and dynamics of scroll waves are analyzed at several points along the line  $b = 0.01$ , as  $a$  varies and crosses the different boundaries.

## B. Numerical strategy

In order to obtain the steady scroll waves and compute their stability spectrum, Eq. (1, 2) are written in cylindrical coordinates with  $u$  and  $v$  functions of  $r, \phi = \theta - \omega t - \tau_w z, t$  and  $z$ ,

$$(\partial_t + 2\tau_w \partial_{\phi z}^2 - \partial_{zz}^2)u = (\omega \partial_\phi + \tau_w^2 \partial_{\phi\phi}^2 + \nabla_{2D}^2)u + f(u, v)/\epsilon \quad (3)$$

$$\partial_t v = \omega \partial_\phi v + g(u, v) \quad (4)$$

### 1. Steady states

A steady scroll wave for a given imposed twist  $\tau_w$  is a time independent solution of Eq. (3, 4) with  $u(r, \phi, t, z) = u_0(r, \phi)$  and  $v(r, \phi, t, z) = v_0(r, \phi)$  and rotation frequency  $\omega = \omega_1$ ,

$$(\nabla_{2D}^2 + \omega_1 \partial_\phi + \tau_w^2 \partial_{\phi\phi}^2)u_0 + f(u_0, v_0)/\epsilon = 0 \quad (5)$$

$$\omega_1 \partial_\phi v_0 + g(u_0, v_0) = 0 \quad (6)$$

This nonlinear fixed point problem for the function  $u_0, v_0$  and nonlinear eigenvalue  $\omega_1$  is solved by using Newton's method after discretization of Eq. (5,6), as detailed in appendix A 1. It should be noted that Eq. (5, 6) are purely two-dimensional due to the scroll wave translation symmetry along the  $z$  axis in the introduced coordinates.

### 2. Linear stability

Once a steady scroll wave is obtained, one can linearize Eq. (3, 4) around it. Invariance of Eq. (3, 4) and of the steady state by translation along the  $z$ -direction (in the introduced twisted rotating frame) leads to decompose a general perturbation depending on the three spatial coordinates on its Fourier components along the  $z$ -axis. We thus consider perturbations under the form  $u = u_0 + \exp[\sigma(k_z)t - ik_z z]u_1(r, \phi), v = v_0 + \exp[\sigma(k_z)t - ik_z z]v_1(r, \phi)$ . The linear equations obeyed by  $u_1, v_1$  and the (complex) growth rate  $\sigma(k_z)$  read,

$$\sigma u_1 = (-k_z^2 + 2i\tau_w k_z \partial_\phi)u_1 + (\omega_1 \partial_\phi + \tau_w^2 \partial_{\phi\phi}^2 + \nabla_{2D}^2)u_1 + [\partial_u f(u_0, v_0)u_1 + \partial_v f(u_0, v_0)v_1]/\epsilon \quad (7)$$

$$\sigma v_1 = \omega_1 \partial_\phi v_1 + \partial_u g(u_0, v_0)u_1 + \partial_v g(u_0, v_0)v_1 \quad (8)$$

or symbolically,

$$\sigma(k_z) \begin{pmatrix} u_1 \\ v_1 \end{pmatrix} = \mathcal{L}_{k_z} \begin{pmatrix} u_1 \\ v_1 \end{pmatrix} \quad (9)$$

So in a second step, the ( $\sim 10$ ) eigenvalues of largest real parts of  $\mathcal{L}_{k_z}$  are precisely determined (for given  $k_z$  and  $\tau_w$ ) using an iterative algorithm [20] detailed in appendix A 2. The whole numerical procedure is quite similar to the spiral linear stability analysis of ref. [21] and extends it to 3D. It should be noted that the twist rate  $\tau_w$  can be prescribed at will so the procedure is not confined to weak twist (of course, for too large a twist, a steady scroll may no longer exist and the Newton steady state finding procedure fails to converge).

Two points are worth emphasizing:

-taking a Fourier transform has eliminated the  $z$ -direction so Eq. (7, 8) are purely two-dimensional (but  $k_z$ -dependent) as the steady state equations (5, 6),

-correlatively, each mode of the 2D-spiral is replaced by a band of modes indexed by the wavevector  $k_z$ .

Some general properties of the spectrum can be noted at this stage.

For zero twist, Eq. (7, 8) depend only on  $k_z^2$  so the spectrum bands are even functions of  $k_z$ . Moreover,  $\mathcal{L}_{k_z}$  is a real operator and its complex eigenvalues come in complex conjugate (c.c.) pairs. So, bands of complex modes also come in complex conjugate pairs.

For non-zero twist ( $\tau_w \neq 0$ ), these symmetries non-longer hold. It only remains true that  $\mathcal{L}_{k_z} = \mathcal{L}_{-k_z}^*$ . So bands of complex modes can be grouped in pairs  $\sigma_1(k_z), \sigma_2(k_z)$  with  $\sigma_2(k_z) = \sigma_1^*(-k_z)$

### 3. Direct numerical simulations and instantaneous filament definition

In order to determine the bifurcation type and the fate of each instabilities, we performed direct numerical simulations of Eq. (1,2) as explained in appendix A 3. In two dimensions, it is usual to define the spiral tip as the intersection point of two (somewhat arbitrary) particular level lines  $u = u_{tip}, v = v_{tip}$ . The spiral tip trajectory is then a convenient way to visualize the spiral dynamics and its core instabilities. Similarly in 3D, we choose here to define the instantaneous filament as the intersection line of the two particular level surfaces  $u = u_{tip} = 0.5$  and  $v = v_{tip} = 0.75(0.5a - b)$ . It can be thought of as the line of spiral tips in the different  $xy$ -plane.

### C. Special eigenmodes

In the 2D case, there are five dominant modes of spiral dynamics in the simple case described by Eq. (1, 2) [22] :  
 -one neutral mode with  $\sigma = 0$ , the rotation mode, which comes from the rotational invariance of Eq. (3, 4).  
 -two complex conjugate purely imaginary modes with  $\sigma = \pm i\omega_1$ , the translation modes, coming from the translation invariance of the starting equations (1, 2)  
 - two complex conjugate modes, the meander modes, corresponding to the oscillatory meander instability the real part of which crosses zero on the meander instability line.

In the following, the five bands of modes originating from these special modes are found to play the most important role in scroll wave dynamics in the sense that they have the largest real parts and that each instability of a scroll wave can be ascribed to one of these bands (i.e. the modes on a part of that particular band acquire a positive real part).

Thus, before proceeding it is worth recalling the expression of these symmetry eigenmodes for spirals [21] and their straightforward generalization for scroll waves.

The rotation mode is the simplest. Differentiation of Eq. (5, 6) directly shows that  $(\partial_\phi u_0, \partial_\phi v_0)$ , the rotation mode, is a solution of Eq. (7, 8) for  $k_z = 0$  and  $\sigma = 0$ .

The eigenmodes associated to invariance under  $x, y$ -translations of the spiral rotation center are less straightforwardly obtained because the spiral is a time independent solution in a rotating frame (with  $(x', y')$  coordinates). A steady spiral rotating around the origin is given by

$$U_0[x', y'] = U_0[\cos(\omega_1 t)x + \sin(\omega_1 t)y, -\sin(\omega_1 t)x + \cos(\omega_1 t)y] \quad (10)$$

The corresponding spiral rotating around the point  $(x_0, y_0)$  is then

$$U_0[\cos(\omega_1 t)(x - x_0) + \sin(\omega_1 t)(y - y_0), -\sin(\omega_1 t)(x - x_0) + \cos(\omega_1 t)(y - y_0)].$$

Using the  $(x', y')$  rotating coordinates, this translated spiral reads,

$$\begin{aligned} U_0[x' - x_0 \cos(\omega_1 t) - y_0 \sin(\omega_1 t), y' + x_0 \sin(\omega_1 t) - y_0 \cos(\omega_1 t)] = \\ U_0[x' - \left(\frac{x_0 - iy_0}{2}\right) \exp(i\omega_1 t) + c.c., y' - \left(i\frac{x_0 - iy_0}{2}\right) \exp(i\omega_1 t) + c.c.] \end{aligned} \quad (11)$$

Expansion of Eq. (11) for small  $x_0, y_0$  gives the expression of the translation modes

$$\begin{pmatrix} u_t \\ v_t \end{pmatrix} = \begin{pmatrix} (\partial_{x'} + i\partial_{y'})u_0 \\ (\partial_{x'} + i\partial_{y'})v_0 \end{pmatrix} = \exp(i\phi) \begin{pmatrix} \partial_r u_0 + i\partial_\phi u_0/r \\ \partial_r v_0 + i\partial_\phi v_0/r \end{pmatrix} \quad (12)$$

with eigenvalue  $i\omega_1$ , and the complex conjugate eigenvector with eigenvalue  $-i\omega_1$ .

This computation immediately generalizes to untwisted scroll waves. This is also the case for twisted scroll waves but one should recall that Eq. (5, 6) are written in a referential that rotates in time but also as one moves along the  $z$ -axis. This modifies the exponential factor in Eq. (11) which becomes  $\exp(i\omega_1 t + \tau_w z)$  to include the  $z$ -rotation. So, for a twisted scroll wave the translation mode  $(u_t, v_t)$  is an eigenvector of  $\mathcal{L}_{k_z=-\tau_w}$  with eigenvalue  $i\omega_1$ . The other (complex conjugate) translation eigenvector  $(u_t^*, v_t^*)$  is associated to the eigenvalue  $-i\omega_1$  of the now *different* linear operator  $\mathcal{L}_{k_z=\tau_w}$ .

A direct algebraic proof of these facts can be given. If ones defines the two operators

$$\begin{aligned} T &\equiv \exp(i\phi)(\partial_r + i/r\partial_\phi) \\ M &\equiv \omega_1\partial_\phi + \tau_w^2\partial_{\phi\phi}^2 + \nabla_{2D}^2 \end{aligned} \quad (13)$$

a direct computation gives the commutators

$$\begin{aligned}[T, M] &= -i\omega_1 T - \tau_w^2 (1 + 2i\partial_\phi) T \\ [T, \partial_\phi] &= -iT\end{aligned}\tag{14}$$

With these notations, the fixed point equations reads  $Mu_0 + f(u_0, v_0) = 0$ ,  $\omega_1 \partial_\phi v_0 + g(u_0, v_0) = 0$ . Action of  $T$  on these two equations gives  $TMu_0 + \partial_u f Tu_0 + \partial_v f Tv_0 = 0$ ,  $\omega_1 T \partial_\phi v_0 + \partial_u g Tu_0 + \partial_v g Tv_0 = 0$ . Commutations of  $T$  and  $M$  (in the first one) and  $T$  and  $\partial_\phi$  (in the second one) using Eq. 14 directly show that  $(u_t, v_t) = (Tu_0, Tv_0)$  satisfies Eq. (7, 8) with  $\sigma = +i\omega_1$  and  $k_z = -\tau_w$ .

#### D. Left eigenvectors and scalar product

The linear stability computation can be extended to determine the left eigenvectors of  $\mathcal{L}_{k_z}$ . We have found it worth in particular to compute the left eigenvectors of the 2D spiral stability operator  $\mathcal{L}$  (i.e.  $\mathcal{L}_{k_z=0}$  for  $\tau_w = 0$ ) corresponding to the translation and rotation modes since they often appear in perturbation calculation [16,12] (for examples, see section III A 1 and appendixD).

We simply define the scalar product between a left  $(\tilde{u}, \tilde{v})$  and right  $(u_r, v_r)$  two-component function by integration over the whole 2D space as  $\langle \tilde{u}, u_r \rangle + \langle \tilde{v}, v_r \rangle$  where

$$\langle f, g \rangle \equiv \iint dr d\phi r f(r, \phi) g(r, \phi) \tag{15}$$

The left eigenmodes of  $\mathcal{L}$  thus obey,

$$\sigma \tilde{u}_1 = (-\omega_1 \partial_\phi + \nabla_{2D}^2) \tilde{u}_1 + \partial_u f(u_0, v_0) \tilde{u}_1 / \epsilon + \partial_u g(u_0, v_0) \tilde{v}_1 \tag{16}$$

$$\sigma \tilde{v}_1 = -\omega_1 \partial_\phi \tilde{v}_1 + \partial_v f(u_0, v_0) \tilde{u}_1 / \epsilon + \partial_v g(u_0, v_0) \tilde{v}_1 \tag{17}$$

The result of one such computation for the left translation eigenmode  $(\tilde{u}_t, \tilde{v}_t)$  (the solution  $(\tilde{u}_1, \tilde{v}_1)$  for  $\sigma = i\omega_1$ ) is shown in Fig. 2. In contrast to the translation mode  $(u_t, v_t)$ , the left eigenmode  $(\tilde{u}_t, \tilde{v}_t)$  quickly decreases away from the spiral core as argued in [12] and explicitly obtained in the free-boundary limit [14,23] (but opposite to what is supposed in [16]). This also holds for the left rotation mode  $(\tilde{u}_\phi, \tilde{v}_\phi)$  (the solution  $(\tilde{u}_1, \tilde{v}_1)$  for  $\sigma = 0$ ) as shown in Fig. 3. As a consequence, the scalar product (15) between these left functions  $(\tilde{u}, \tilde{v})$  and any right function  $(u_r, v_r)$  (even slowly increasing) is well defined<sup>1</sup>. We do not find it useful to include a time integration in the scalar product as in [16,12].

### III. UNTWISTED FILAMENTS

We begin with the simplest case of scroll waves with no twist ( $\tau_w = 0$ ). In this case, the steady scroll equations (5, 6) are clearly identical to those of a 2d spiral. We take as an example the parameter value  $a = 0.9$ ,  $b = 0.01$  (and  $\epsilon = 0.025$ ). A steady spiral/scroll wave is found for a rotation frequency  $\omega_1 = 1.769$ . The linear spectrum of modes around this steady scroll is plotted in Fig. 4 (only the upper quadrant upper  $k_z > 0$ ,  $Im(\sigma) > 0$  is shown since the other quadrants can be deduced by parity and complex conjugation) The five translation, rotation and meander modes of the spiral wave stand at  $k_z = 0$ . The steady spiral is stable as shown by the negative real parts of the meander modes. As stated above, the spectrum around the scroll wave is organized in several bands of modes which originates from the spiral modes at  $k_z = 0$ . Only the five less stable bands are shown in Fig. 4. At these parameter values, extension to the third dimension does not bring any instability (at least at the linear level) since as seen on Fig. 4 the real part of  $\sigma(k_z)$  becomes more negative on each band as  $k_z$  increases. For other parameter values, a straight scroll wave can however be unstable while 2D-spiral are stable. This can happen in two different ways. Depending on position in parameter space, either the translation or the meander bands become unstable for  $k_z \neq 0$ . We examine these two cases in turn in the following two subsections.

---

<sup>1</sup>The fast decay of the left eigenmodes makes the space integration converge without any additional factor. Adding one such extra factor as suggested in [16] would actually make all the scalar product vanish.

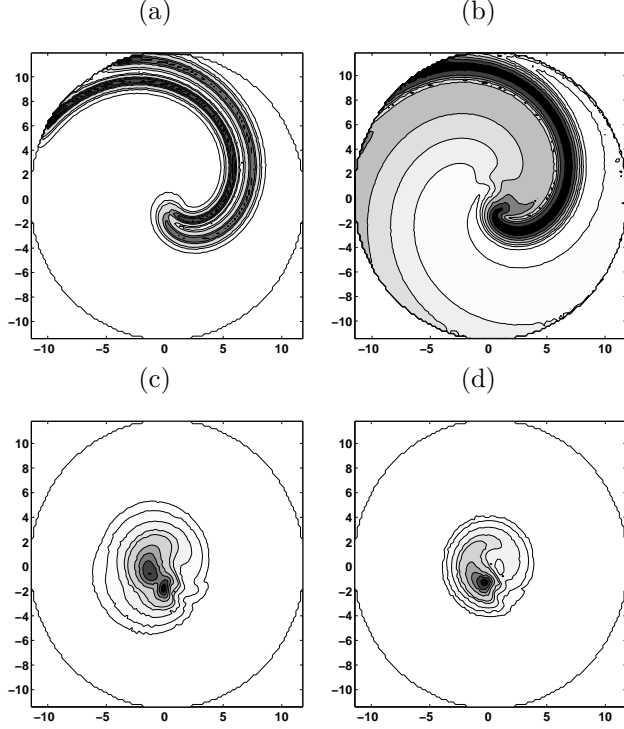


FIG. 2. Contour plots of the translation eigenmode, (a)  $u$ -component modulus, (b)  $v$ - component modulus, and of the corresponding left eigenvector , (c)  $u$ -component modulus, (d)  $v$ - component modulus. The maximum value of the fields is set independently for  $u$  and  $v$  equal to 1. and the contours are plotted for (a) $u = 0.01, 0.05, 0.1, 0.3, 0.4, 0.5, 0.6$  and  $0.7$ , (b) $v = 0.01, 0.05, 0.1, 0.2, 0.4, 0.6$  and  $0.8$ , (c) and (d)  $u, v = 0.0001, 0.001, 0.01, 0.05, 0.1, 0.3, 0.5, 0.7$  and  $0.9$ . The parameter values are  $a = 0.44$ ,  $b = 0.01$  and  $\epsilon = 0.025$ . The pulsation of the steady rotating spiral is  $\omega = 1.1612$ . The circles represent the limit of the simulation box.

### A. Translation band instability

The translation bands can have unstable modes for  $k_z \neq 0$  while the 2D spirals are stable. An example of this phenomenon is shown on Fig. 5 for  $a = 0.44$ ,  $b = 0.01$  and  $\epsilon = 0.025$ . A qualitatively similar spectrum is obtained for all points in Fig. 1 denoted by filled dots ( $\bullet$ ) near the large core spiral existence boundary  $\partial R$ . As seen on Fig. 5, the instability takes place for small  $k_z$  as soon as  $k_z$  is non-zero. It corresponds to the "negative line tension" instability of ref. [12]. We show below that the curvature of the translation modes at  $k_z = 0$  is given by the spiral drift coefficients in an external field. So, this translation band instability is directly related to the fact that 2D spiral drift opposite to an applied external field in this parameter region.

#### 1. Long wavelength stability and 2d spiral drift in an external field

As recalled and shown in detail in appendix B, a small applied external field  $E$  induces a drift of the spiral rotation center at a velocity  $v$  such that

$$v = \alpha_{\parallel} E + \alpha_{\perp} \omega_1 \times E \quad (18)$$

where  $\omega_1$  is the spiral rotation vector. It has previously been noted [14] that a weak scroll wave curvature acts as an external field and therefore that a straight scroll wave is unstable if  $\alpha_{\parallel} < 0$  since a small curvature tends to grow. More precisely, the small  $k_z$  behavior of the two translation bands is given by

$$\sigma_{\pm}(k_z) = \pm i\omega_1 + (-\alpha_{\parallel} \pm i\alpha_{\perp}) k_z^2 + O(k_z^4) \quad (19)$$

Eq. (19) is simply derived by a first-order perturbative calculation as follows. The linear eigenvalue problem (7, 8) reads

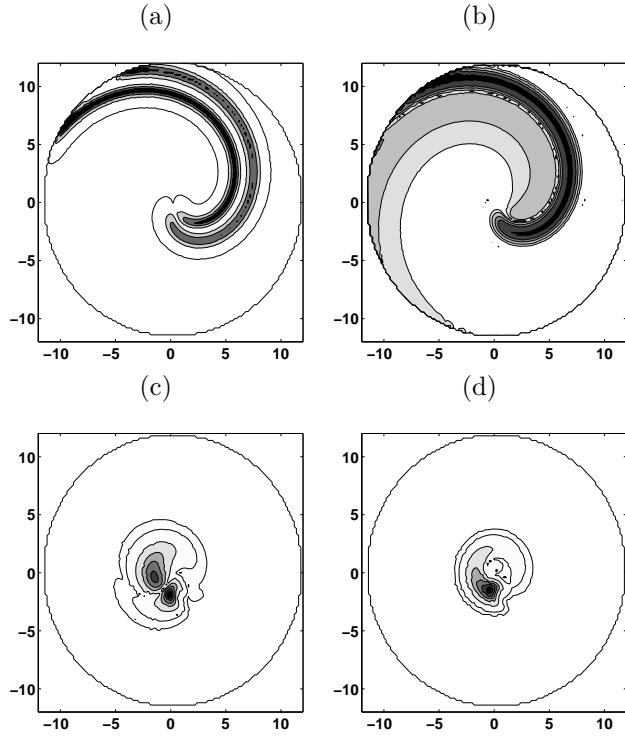


FIG. 3. Contour plots of the rotation eigenmode, (a)  $u$ -component modulus, (b)  $v$ - component modulus, and of the corresponding left eigenvector , (c)  $u$ -component modulus, (d)  $v$ - component modulus. The maximum value of the fields is set equal to 1. and the contours are plotted for (a)  $u = 0.001, 0.1, 0.3, 0.5$  and  $0.7$ , (b)  $v = 0.001, 0.1, 0.2, 0.4, 0.6$  and  $0.8$ , (c) and (d)  $u, v = 0., 0.001, 0.01, 0.1, 0.3, 0.5, 0.7$  and  $0.9$ . Same parameters as in Fig. 2.

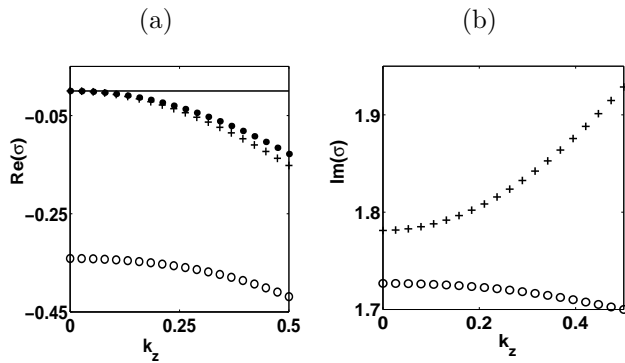


FIG. 4. (a) Real and (b) imaginary parts of the growth rate  $\sigma(k_z)$  as a function of the wavenumber  $k_z$  for the translation (+), rotation ( $\bullet$ ) and meander ( $\circ$ ) bands. The parameter values are  $a = 0.9$ ,  $b = 0.01$  and  $\epsilon = 0.025$ . Fig. 4a shows that the meander mode at  $k_z = 0$  is stable and that the growth rate decreases on the meander band with  $k_z$ . The translation mode is also restabilized for finite values of  $k_z$ . The translation and meander bands are well approximated by respectively  $\sigma_t(k_z) = i1.769 + (-0.65 + i0.61)k_z^2$  and  $\sigma_m(k_z) = -0.3411 + i1.720 + (-0.25 + i0.01)k_z^2$ . The value of  $\sigma_t(0)$  is in good agreement with the independently determined pulsation of the steady scroll wave  $\omega_1 = 1.769$

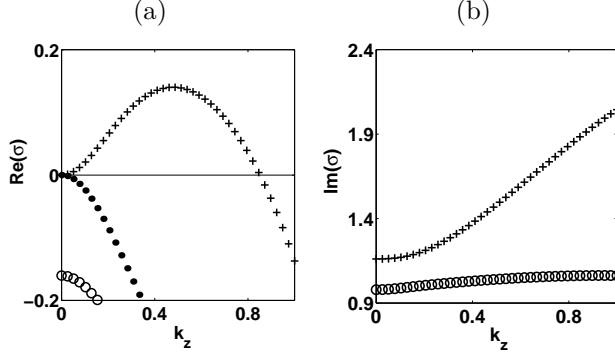


FIG. 5. (a) Real and (b) imaginary part of the growth rate  $\sigma(k_z)$  as a function of the wavenumber for the parameter value  $a = 0.44$ ,  $b = 0.01$ ,  $\epsilon = 0.025$ . The meander mode, (○) is stable and the growth rate decreases with the wave number on the meander band. The modes of the rotation band (●), are also stable. The mode of the translation band (+), are unstable for finite values of  $k_z$ .

$$\sigma(k_z) \begin{pmatrix} u_1 \\ v_1 \end{pmatrix} = -k_z^2 \begin{pmatrix} u_1 \\ 0 \end{pmatrix} + \mathcal{L}_{k_z=0} \begin{pmatrix} u_1 \\ v_1 \end{pmatrix}. \quad (20)$$

For small  $k_z$ , the modes of the translation bands can be obtained by perturbation around the known translation modes at  $k_z = 0$  (Eq. 12). For definiteness, we consider the upper band (which start at  $\sigma(k_z = 0) = +i\omega_1$ ) and write  $\sigma(k_z) = i\omega_1 + \delta\sigma$  where  $\delta\sigma \ll 1$  is the sought perturbative correction,

$$\begin{pmatrix} u_1 \\ v_1 \end{pmatrix} = \begin{pmatrix} u_t \\ v_t \end{pmatrix} + \begin{pmatrix} \delta u_1 \\ \delta v_1 \end{pmatrix} \quad (21)$$

Substitution in Eq. (20) gives

$$\delta\sigma \begin{pmatrix} u_t \\ v_t \end{pmatrix} + i\omega_1 \begin{pmatrix} \delta u_1 \\ \delta v_1 \end{pmatrix} = -k_z^2 \begin{pmatrix} u_t \\ 0 \end{pmatrix} + \mathcal{L}_{k_z=0} \begin{pmatrix} \delta u_1 \\ \delta v_1 \end{pmatrix} \quad (22)$$

The first-order expression of  $\delta\sigma$  is obtained in a usual way by taking the scalar product of Eq. (22) with the left eigenvector  $(\tilde{u}_t, \tilde{v}_t)$  of  $\mathcal{L}_{k_z=0}$  for the eigenvalue  $i\omega_1$  (section II D)

$$\delta\sigma = -k_z^2 \frac{\langle \tilde{u}_t, u_t \rangle}{\langle \tilde{u}_t, u_t \rangle + \langle \tilde{v}_t, v_t \rangle} \quad (23)$$

Eq. (23) is equivalent to the announced formula (19) since the matrix coefficients on its r.h.s also gives the spiral drift coefficients, as shown in appendix B (see Eq. (B10)).

In Table I, the spiral drift coefficients  $\alpha_{\parallel}$  and  $\alpha_{\perp}$  are compared to the results of independent computations of the curvature of  $\sigma(k_z)$  at  $k_z = 0$  for the translation bands, from diagonalisations of  $\mathcal{L}_{k_z}$  at different values of  $a$ . The good agreement between these results is a check both of the analytic formula (19) and of our numerics. To recapitulate, the translation band instability is found to be a long wavelength instability (i.e. the band of unstable wavelength starts at  $k_z = 0$ ) which is present in the whole domain of parameters where a 2D-spiral drifts opposite (given our sign convention in Eq. B1) to the applied field.

## 2. Nonlinear evolution of the instability

The nonlinear fate of this translation band instability was studied by direct dynamical simulations of Eq. (1, 2). In the parameter regime of Fig. 5 when modes of the translation bands are unstable for finite values of  $k_z$ , an initially straight scroll wave was observed to be unstable provided that the simulation box was large enough to accommodate an unstable mode. In agreement with previous observations [12], the filament was observed to increasingly depart from its straight initial configuration and its length was observed to grow in the simulation box. When the filament eventually collided with the boundaries of the simulation box, it split into two filaments. This repeated again and no

$a$	$\omega_1$	$\sigma_t''(k_z = 0)/2$	$\sigma_m''(k_z = 0)/2$	$\alpha_{\parallel} - i\alpha_{\perp}$
0.44	1.16	$1.9 + 0.82i$	$-1.6 + 0.78i$	$-1.97 - 0.84i$
0.48	1.38	$3.2 + 0.44i$	$-3.7 + 1.10i$	$-3.0 - 0.49i$
0.67	1.76	$-2.14 + 0.85i$	$1.61 + 0.25i$	$2.2 - 0.9i$
0.7	1.78	$-1.63 + 0.83i$	$1.04 + 0.21i$	$1.62 - 0.83i$
0.8	1.81	$-0.87 + 0.70i$	$0.08 - 0.06i$	$0.854 - 0.71i$
0.9	1.77	$-0.65 + 0.61i$	$-0.25 - 0.089i$	$0.66 - 0.61i$

TABLE I. The scroll wave pulsation  $\omega_1$ , half the second derivative  $\sigma_t''(k_z = 0)/2$  of the translation band at  $k_z = 0$  (with  $\sigma_t(0) = i\omega_1$ ), half the second derivative  $\sigma_m''(k_z = 0)/2$  of the meander band at  $k_z = 0$  (with  $Im(\sigma_m(0)) > 0$ ) and the drift coefficients of the 2D-spiral in an electric field  $\alpha_{\parallel} - i\alpha_{\perp}$  for  $b = 0.01$ ,  $\epsilon = 0.025$  and different values of  $a$ .

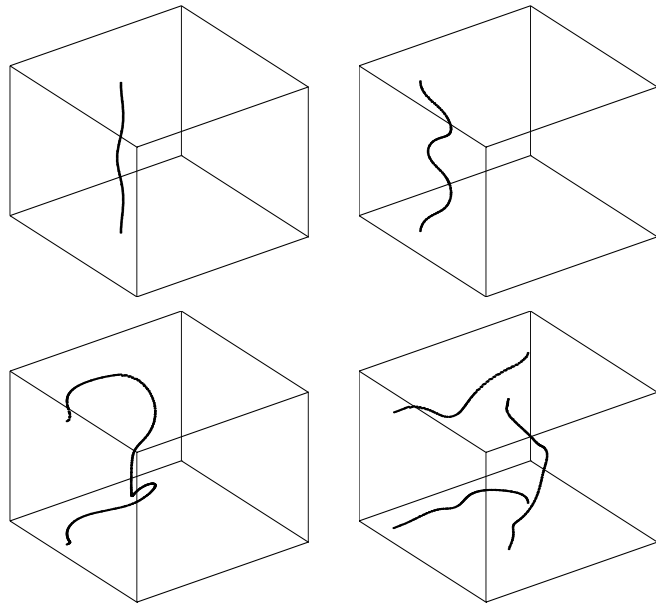


FIG. 6. Instantaneous filament evolution starting from a slightly perturbed straight scroll for equally spaced times ( $t = 25.$ ,  $t = 50.$ ,  $t = 75.$  and  $t = 100.$ ) during a simulation in a simulation box of size  $(128 \times 128 \times 120)$  with a space discretization step  $dx = 0.2$  using periodic boundary conditions. The parameters are  $a = 0.44$ ,  $b = 0.01$  and  $\epsilon = 0.025$  and correspond to the linear spectrum shown in Fig. 5.

restabilisation was observed. A typical evolution is shown in Fig. 6. The minimum simulation box size which allowed the instability development closely agreed with the results of the linear stability analysis. For instance, in the case  $a = 0.44$ ,  $b = 0.01$ , and  $\epsilon = 0.025$ , the maximal  $k_z$  of the unstable band is obtained to be  $k_z = 0.84$  via the linear stability analysis whereas the direct numerical simulations show a minimal simulation box height corresponding to  $k_z = 0.81$ <sup>2</sup>.

The choice of boundary conditions on the simulation box top and bottom faces influences the minimum box height for the instability development (but, apart from that, was not observed to qualitatively modify the instability nonlinear development). This critical size was found to be twice bigger for periodic periodic boundary condition than for no-flux boundary conditions which can accommodate linear modes of wavelength twice as long as the box height.

## B. The third dimension-induced meander instability

In the region where a 2D-spiral drifts toward an applied field (i.e.  $\alpha_{\parallel} > 0$ ), the modes of an untwisted scroll wave translation bands are stable. As pointed in [15], an untwisted scroll wave can nonetheless be unstable in a parameter region where a 2D-spiral is stable. This happens when the meander bands are destabilized by deformation in the  $z$ -direction as we study below.

### 1. Linear analysis

This induction of the meander instability by three-dimensional effects is shown in Fig. 7. For the parameters of Fig. 7a, all modes have negative real parts and the scroll wave is stable. However, one sees that the real part of the modes on the meander band starts by increasing as  $k_z$  increases from zero. For the parameters of Fig. 7b which stand closer to the 2D meander boundary, a finite band of modes with  $k_z \neq 0$  has acquired a positive real part while the real part of 2D spiral meander mode at  $k_z = 0$  is still negative. Thus, for these parameter values close to the "small core" side of the 2D meander instability boundary, a 3D scroll wave is unstable to meander while the steadily rotating 2D spiral is still stable as pointed out in [15]. On the "large core" side of the meander instability boundary,

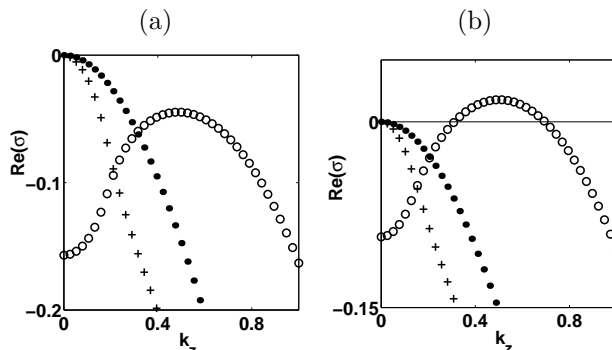


FIG. 7. The growth rate  $Re[\sigma(k_z)]$  as a function of the wavenumber for the parameter value (a)  $a = 0.7$  and (b)  $a = 0.67$  (b). The other parameter are  $b = 0.01$  and  $\epsilon = 0.025$ . The meander mode, (o), is stable for  $k_z = 0$  both in cases (a) and (b). The growth rate increases on the meander band with  $k_z$ . In case (a), it always remains negative and there is no instability. In case (b), it becomes positive for  $k_z$  higher than 0.30 and lower than 0.69 showing the finite- $k_z$  instability of the steady scroll wave. The rotation (●) and translation bands (+) are stable. In the phase diagram Fig.1 the points with a spectrum similar to the (b) case are represented by crosses (×).

three-dimensional modulations have on the contrary a stabilizing effect on the meander instability and the 2D and 3D meander instability thresholds coincide as shown on Fig 8 (note however that the translation band instability of section III A renders the scroll wave unstable for these parameters). The fact that the curvature of the translation

<sup>2</sup>For the observed largest unstable  $k_z$ , numerical simulations were not carried long enough to observe the full nonlinear development of the instability. However, it was observed with a box height increase of a single space step.

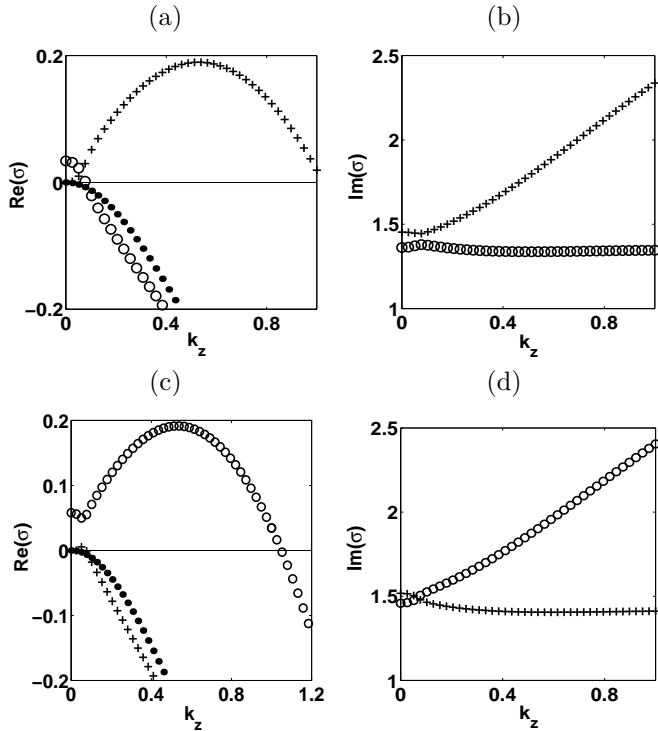


FIG. 8. Real and imaginary part of the growth rate  $\sigma(k_z)$  as a function of the wavenumber for  $b = 0.01$ ,  $\epsilon = 0.025$ . (a), (b):  $a = 0.5$ ; (c), (d):  $a = 0.52$ . In both cases, the real part decreases on the meander band and increases on the translation band with  $k_z$  for small values of  $k_z$ . In the  $a = 0.52$  case, hybridization of the eigenvectors of the two bands exchange these trends at slightly higher values of  $k_z$  i.e. the real part of the meander band increases whereas the real part of the translation band decreases. In the phase diagram of Fig. 1, the points where the linear spectrum is similar to one of these cases (with both the meander and translation bands unstable at small  $k_z$ ) are represented by circles (○).

and meander bands are of opposite sign in Fig. 5 and Fig. 7 may lead to think that the finite  $k_z$  behavior of the meander bands is also related to 2D spiral drift (as indeed proposed in [15]). However, a quantitative computation shows no simple relation between the meander bands curvature at  $k_z = 0$  and the spiral drift coefficient as reported in table I. Moreover, even at the qualitative level, there is no general validity to the opposite sign rule between the translation and meander bands curvature at  $k_z = 0$ , as shown by the data of Fig. 4.

It is of some interest to see how the spectrum of Fig. 5 is transformed into the spectrum of Fig. 7 as one traverses the 2D meander unstable region. This happens through hybridization between the translation and meander bands as illustrated in Fig. 8.

## 2. Restabilized bifurcated states

We performed direct numerical simulations to examine the nonlinear development of the meander bands instability at  $k_z \neq 0$  and to characterize the restabilized nonlinear states. For boxes of medium size in the  $z$ -direction as used in our numerical simulations, the restabilized nonlinear states strongly depend on the top and bottom boundary conditions. Two different ones were implemented (no flux boundary conditions were always implemented on the side boundaries). We used either periodic boundary conditions which permit the development of a single pair of unstable modes and are simpler to analyze or no-flux boundary conditions since they are clearly more relevant in an experimental context. We describe the results in turn.

### Periodic boundary conditions.

Direct numerical simulations were performed in the parameter regime of Fig. 7. Three types of initial conditions were used which all led to a stationary restabilized scroll wave after a transient regime.

For the first one, the perturbation of the steady state was chosen to contain the unstable wavelengths  $\pm k_z$ . The initial fields were chosen in the form  $u(x, y, z) = u_{2D}(x, y)(1 + \alpha \cos(k_z z))$ ,  $v(x, y, z) = v_{2D}(x, y)(1 + \alpha \sin(k_z z))$  with

the magnitude  $\alpha$  of the 3D perturbation being of order  $10^{-2}$  ( $u_{2D}$  and  $v_{2D}$  correspond to a steady spiral wave which is stable in 2D in this regime). This perturbation transforms the straight unperturbed instantaneous filament into an "helix" of small elliptical cross section and pitch  $2\pi/k_z$ . When the wavelength  $k_z$  corresponded to an unstable mode, this helix was observed to grow and to reach a helical restabilized state of periodicity  $k_z$ .

A slightly more complicated time development was observed with an initial perturbation of the straight scroll wave in the form  $u(x, y, z) = u_{2D}(x, y)(1 + \alpha \cos(k_z z))$ ,  $v(x, y, z) = v_{2D}(x, y)(1 + \alpha \cos(k_z z))$ . This gives the instantaneous filament  $(x_f(z), y_f(z))$  a planar "zig-zag" shape of small amplitude,  $x(z) = x_1 \cos(k_z z)$ ,  $y(z) = y_1 \cos(k_z z)$ . The zig-zag perturbation was first observed to grow before turning into an helical restabilized state of periodicity  $k_z$ . This type of time development is expected on general ground in system where left and right progressive wave compete (see e.g. [24]).

Finally, competition between several different unstable modes (up to 4 different  $k_z$ ) was examined with initial conditions such as  $u(x, y, z) = u_{2D}(x, y)[1 + \alpha \exp(-(z - z_o)^2/L_c)]$ ,  $v(x, y, z) = v_{2D}(x, y)[1 + \beta \exp(-(z - z_o)^2/L_c)]$ . (typical values are  $\|(\alpha, \beta)\|_2 = 0.01$  and  $L_c$  about a few tens of space steps). In that case, it was generally observed that the most unstable wavelength compatible with the box height was selected. At a qualitative level, the transient regime was found to mainly depend of the planar or non planar character of the initial perturbed filament : When it was planar (case  $\beta = \alpha$ ) a zig-zag filament first grew before taking an helical shape. When it was non planar,  $\beta \neq \alpha$  then an helical filament grew directly.

Close to the instability threshold, the shape of the restabilized instantaneous filament is closely approximated by an helix of circular cross section, as shown in Fig. 9, and its motion can be portrayed in a way similar to the epicycle description of meander. The axis of the instantaneous filament helix rotates around a fixed vertical axis at the frequency of the steady two dimensional spiral. In the rotating frame where these two axes are fixed, the helical instantaneous filament itself rotates with a frequency close to the imaginary part of the meander linear eigenmode (i.e. the difference between these two frequencies is of order  $10^{-2}$  in a strong meander regime and of order  $10^{-3}$  in a weak meander regime). Thus, for periodic boundary conditions the meander amplitude is found to be independent of height ( $z$ ) while the phase of the epicycle motion varies linearly with  $z$ .

We performed two different systematic studies in order to better characterize the nature of the 3D meander bifurcation. In the first one, we kept the size of the simulation box constant and varied the excitability using  $a$ . In the second one, we kept  $a$  constant and varied the size of the simulation box, that is the wavenumber of the initial perturbation.

At the linear level, the results of these direct numerical simulations are in close agreement with the predictions of the linear stability analysis, both for the the instability threshold  $a_c$  (with an accuracy of order  $10^{-3}$ ) and for the unstable wavenumber range  $[k_-(a), k_+(a)]$ .

The radius of the instantaneous filament helix can be taken as a measure of the 3D meander instability amplitude. As shown in Fig. 10, it is found to behave as the square root of the distance to the threshold (either  $|a - a_c|$  or  $|k_z - k_{\pm}(a)|$ ). Therefore as reported previously [15], the 3D meander bifurcation is a supercritical Hopf bifurcation, as in 2D.

However, the  $k_z$  dependence of the nonlinear term quickly becomes important away from threshold. In Fig. 10, the square of the meander amplitude  $R^2$  is compared to the growth rate of the unstable meander mode in the whole band  $[k_-(a), k_+(a)]$ . A clear asymmetry of the  $R^2$  curve is already seen, with a slope at the  $k_-(a)$ -end about 3.4 times larger than the  $k_+(a)$ -end slope.

*No flux boundary conditions.* For the box height  $H$  used in our simulation (about 2 or 3 unstable wavelengths), the boundary conditions chosen on the top and bottom boundary conditions have a strong influence on the restabilized state. For no-flux boundary conditions, the spiral wave in each horizontal  $xy$ -plane has a meandering motion. However, contrary to the case of periodic boundary conditions the meander amplitude depends on  $z$  and is well approximated by  $|\cos(k_z z)|$  (see Fig. 9). This implies in particular that in some horizontal planes the meander amplitude is zero and that the corresponding spiral tip performs a simple steady rotation. In the rotating frame where these special tips are motionless, the instantaneous filament takes a planar zig-zag shape that rotates around its vertical midline at a pulsation close to the imaginary part of the unstable meander eigenmode corresponding to the wavelength of the filament. Thus, for no-flux boundary condition, the meander amplitude varies sinusoidally with height while the phase of the epicycle motion is independent of height.

This shape and motion are simply understood in a weakly nonlinear description where the restabilized state can be approximated as a sum of the unperturbed solution and the four unstable meander eigenmodes ( $\sigma_m(k_z)$  and  $\sigma_m^*(k_z)$  at  $\pm k_z$ )

$$u = u_0(r, \psi) + [Au_1(r, \psi) e^{i(k_z z + \omega_2 t)} + Bu_1(r, \psi) e^{i(-k_z z r + \omega_2 t)} + c.c.] \quad (24)$$

$$v = v_0(r, \psi) + [Av_1(r, \psi) e^{i(k_z z + \omega_2 t)} + Bv_1(r, \psi) e^{i(-k_z z + \omega_2 t)} + c.c.] \quad (25)$$

with  $u_1, v_1$  the eigenmode of eigenvalue  $\sigma_m(k_z)$  and  $\omega_2 = \text{Im}[\sigma_m(k_z)]$  the meander frequency. The no-flux boundary

condition,  $\partial_z u = 0$ , at  $z = 0$  and  $z = H = 2\pi/k_z$  enforces  $A = B$  (i.e. for the height considered, the no-flux boundary conditions stabilize the state with symmetric upward and downward propagating deformation which was observed to be unstable with periodic boundary conditions). The instantaneous filament corresponding to the fields (25) is easily determined by remembering that it is the locus  $u = u_{\text{tip}}$ ,  $v = v_{\text{tip}}$ . Its position is conveniently parameterized as  $x'_{\text{tip}}(z) = x'_0 + \delta x'(z, t)$ ,  $y'_{\text{tip}}(z) = y'_0 + \delta y'(z, t)$  using Cartesian coordinates in the rotating frame where the unperturbed filament is standing at  $(x'_0, y'_0)$ . For small  $|A|$ , one obtains

$$\partial_x u_0 \delta x' + \partial_y u_0 \delta y' + \cos(k_z z)[2A u_1 e^{i\omega_2 t} + \text{c.c.}] = 0 \quad (26)$$

$$\partial_x v_0 \delta x' + \partial_y v_0 \delta y' + \cos(k_z z)[2A v_1 e^{i\omega_2 t} + \text{c.c.}] = 0 \quad (27)$$

where the field  $u_1, v_1, u_0, v_0$  and their derivatives are evaluated at the unperturbed filament position  $(x'_0, y'_0)$ . Inversion of Eq. (26, 27) gives

$$\begin{aligned} \delta x' &= \cos(k_z z)[\alpha A e^{i\omega_2 t} + \text{c.c.}] \\ \delta y' &= \cos(k_z z)[\beta A e^{i\omega_2 t} + \text{c.c.}] \end{aligned} \quad (28)$$

where  $\alpha$  and  $\beta$  are complex constants which depend on  $u_1, v_1$  and the derivatives of  $u_0$  evaluated at the point  $(x_0, y_0)$ . This clearly shows the planar zig-zag shape of the instantaneous filament since points in different  $xy$ -planes simply differ by the real scale factor  $\cos(k_z z)$ . As time evolves, Eq. 28 also shows that the filament points follow scaled ellipses in different  $xy$ -planes. Our simulations show that, as for 2D meander, these ellipses are in fact almost circular<sup>3</sup>.

Finally, we briefly discuss the transition between the restabilized meander regime seen on the "small core" side of the phase diagram (Fig. 1) and the negative line tension dynamics which belongs to its meander "large core" side. Since scroll waves do meander in this transition region, the evolution of scroll waves as seen in direct numerical simulations is not directly linked to the linear spectrum of the steady scroll wave. For example, when the meander and translation bands are strongly hybridized, the translation bands are only unstable for small values of  $k_z$  (Fig. 8). Nonetheless, direct simulations show that the meandering scroll is unstable and that its core grows as in the negative line tension regime in simulation boxes small enough to only contain unstable modes of the meander bands with larger values of  $k_z$ . This happens on the whole small  $a$  side of the dashed  $\omega_1 = \omega_2$  line of Fig. 1. This line stands very close to the line where the external field drift of meandering spiral changes sign [25] and it is difficult to distinguish the two in our simulations. So, the link between the spiral drift sign and the "negative line tension" type of instability development continues to hold for meandering scroll wave.

#### IV. INFLUENCE OF TWIST

As noted in several previous studies [7,8,10], twist is an important degree of freedom brought by the extension to 3D. It is well-known from classic studies of elasticity [26] (and everyday experience) that straight rods and ribbons can be destabilized by twisting them beyond a certain level. A somewhat similar instability was reported in ref. [10] in numerical simulations of excitable filaments. Beyond a threshold twist, the rotation center line of an initially straight twisted filament was observed to adopt an helical configuration. Observations of a similar 'sproing' [10] instability have since been made in the related context of the complex Ginzburg-Landau equation vortex lines [27]. The characteristics of the excitable filament sproing instability have however remained somewhat unclear. In the dynamical simulations of ref. [10], a single filament turn was imposed in a simulation box with periodic conditions. and the box height was varied. A complicating feature of this procedure is that both twist and the available wavelength range are changed at the same time. On the theoretical side, the instability fails to be captured by small twist approaches [16,12] since [12] the motion of the rotation center is not influenced by twist in this limit (see appendix D).

---

<sup>3</sup>An explanation can be provided by the proximity of the  $\omega_2 = \omega_1$  point on the meander threshold line (as noted in a particular limit in [14]). The argument is that i) the meander modes are close to the translation modes when  $\omega_2$  is close to  $\omega_1$  ii) the ellipse should reduce to a circle for translations since the translated circular core is circular. This can be explicitly seen from Eq. (28). Namely, Eq. (28) gives  $\delta x' + i\delta y' = \cos(k_z z)[A(\alpha + i\beta) \exp(i\omega_2 t) + A^*(\alpha^* + i\beta^*) \exp(-i\omega_2 t)]$ . The explicit inversion of Eq. (26, 27) shows that  $\alpha + i\beta$  is proportional to  $(v_t u_1 - u_t v_1)$  and therefore vanishes when  $(u_1, v_1)$  tends toward the translation eigenmode  $(u_t, v_t)$ . In this limit, it only remains the term proportional to  $\alpha^* + i\beta^*$  and  $\delta x' + i\delta y'$  follows a circle.

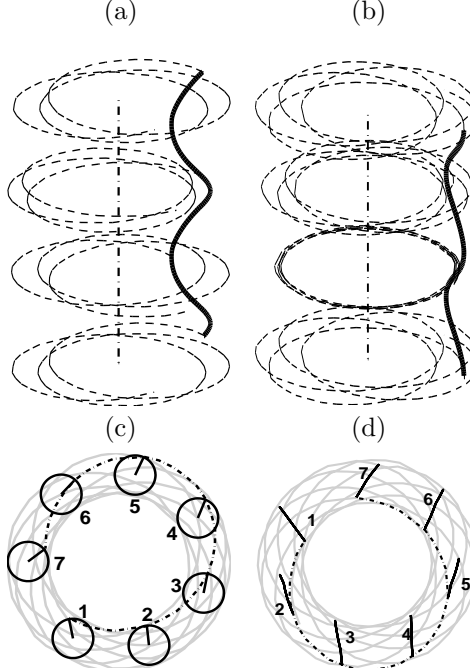


FIG. 9. (a): view of the restabilized state in the weakly non linear regime. The parameters are :  $a = 0.684$ ,  $b = 0.01$  and  $\epsilon = 0.025$ , the size of the simulation box is  $(128 \times 128) \times 130$  with  $dx = 0.2$  and periodic boundary conditions are used. The dashed lines are the trajectories of the tip of the spiral in four regularly spaced horizontal planes. The bold line is the instantaneous helical filament. The dash-dotted line is the axis around which the axis of the helical filament rotates. (c): black bold circles, projections of the instantaneous filament on an horizontal plane at different times. The bold radius in each circle shows the instantaneous filament point at height  $z = 0$ . This point trajectory is also shown for several periods of rotation (bold dashed-dotted line: evolution between circles 1 and 7; thin gray line: evolution for some time afterwards). The pulsation of the axis of the filament is equal to  $\omega_1 = 1.744$ , the pulsation of the meander in the rotating frame is equal to  $\omega_2 = -2.159$ . These values are to be compared with results of the linear stability analysis :  $\omega_1 = 1.766$  and  $\omega_2 = \pm 2.194$ . (b): view of the restabilized state with the same parameters and same simulation box using no flux boundary conditions. The instantaneous filament has a zig-zag shape and the amplitude of meander varies with  $z$ . (d) : black bold lines, projections in an horizontal plane of the instantaneous filament at different times. The trajectory of the spiral tip in a plane where the amplitude of meander is maximal is also shown for several periods of rotation (bold dashed-dotted line: evolution between filaments 1 and 7; thin gray line: evolution for some time afterwards). Its pulsation is equal to  $\omega_1 = 1.745$  whereas the pulsation of the instantaneous filament in the rotating frame is equal to  $\omega_2 = -2.159$ . The mean distance between the instantaneous filament points and the central (dash-dotted) axis is  $R_0 = 0.4930$  in the (a) (periodic boundary condition) figure and  $R = 0.4944$  in the (b) no-flux case. The core radius of the corresponding 2D spiral is  $R_0 = 0.4833$ .

The present approach permits to relieve some of these problems since the twist  $\tau_w$  can be varied from zero to large values and a whole range of wavelengths can be examined in the linear stability computations ( $k_z$  is simply a parameter which can be given any chosen value independently of  $\tau_w$ ).

We restrict ourselves here mostly to parameter values for which a straight untwisted filament is stable, that is on the large  $a$  side of the (3D) meander instability region. Fig. 11 shows the frequency and tip radius for a family of twisted scroll wave obtained by increasing  $\tau_w$  from 0 to  $\tau_w$  at one such parameter point ( $a = 0.8$ ,  $b = 0.01$ ,  $\epsilon = 0.025$ ). The frequency  $\omega_1(\tau_w)$  increases quadratically at small twist and almost linearly for larger twist values. The quadratic behavior at small  $\tau_w$  is simply obtained by applying first order perturbation theory to Eq. (5, 6) which gives

$$\omega_1(\tau_w) = \omega_1(\tau_w = 0) - \tau_w^2 \frac{\langle \tilde{u}_\phi, \partial_{\phi\phi} u_0 \rangle}{\langle \tilde{u}_\phi, \partial_\phi u_0 \rangle + \langle \tilde{v}_\phi, \partial_\phi v_0 \rangle} + O(\tau_w^4) \quad (29)$$

The direct computation of the matrix element ratio on the r.h.s. of Eq. (29) is in good agreement with a direct fit of the  $\omega_1(\tau_w)$  curve of Fig. 11 (see caption). Analytic descriptions of the  $\omega_1(\tau_w)$  curve for larger twist values have recently been obtained in the free boundary limit ( $\epsilon \rightarrow 0$ ) both for small core [28] and large core scroll waves [29].

The determination of a family of increasingly twisted steady scroll waves permits to determine the evolution of the

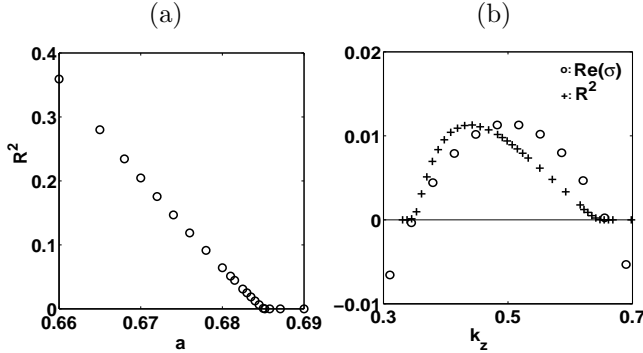


FIG. 10. (a) : square of the amplitude of the meandering restabilized state as a function of the parameter  $a$ . The parameters used are  $b = 0.01$  and  $\epsilon = 0.025$ . The simulation box is  $(128 \times 128) \times 130$ , with  $dx = 0.2$  and periodic boundary conditions are used. (b) : comparison of the square of the amplitude of the meandering restabilized state  $R^2$  multiplied by 0.035 and the growth rate of the meandering mode  $\text{Re}(\sigma)$ . Same parameter regime as in (a) and  $a$  is fixed to 0.68.

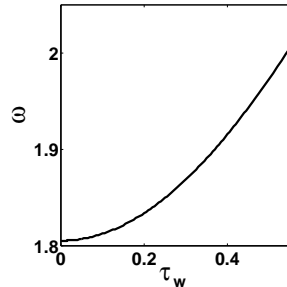


FIG. 11. Frequency  $\omega_1$  of the scroll wave as a function of the twist for  $a = 0.8$ ,  $b = 0.01$ , and  $\epsilon = 0.025$ . The small  $\tau_w$  behavior of the pulsation can be well approximated by  $\omega_1(\tau_w) = \omega_1(\tau_w = 0) + 0.7205\tau_w^2$  for low values of  $\tau_w$ . For higher values of  $\tau_w$ , a linear behavior of  $\omega_1$  as a function of  $\tau_w$  is observed. The first-order perturbation result coefficient (29) is 0.7203 using the numerically determined rotation eigenmodes of  $\mathcal{L}$  and of its adjoint.

stability spectrum with  $\tau_w$ . The results of such a computation are shown in Fig. 12 for scroll waves of Fig. 11. As twist increases, the deformations of the translation bands are particularly important. As expected from general arguments (section II B 2), for  $\tau_w = 0.2$  (Fig. 11b), the translation bands  $\sigma_{t,1}, \sigma_{t,2}$  are no longer even and related by complex conjugation. It only remains the lower symmetry  $\sigma_{t,1}^*(k_z) = \sigma_{t,2}(-k_z)$ . One can note also that the translation modes with  $Re[\sigma(k_z)] = 0$  stand at  $k_z = \pm\tau_w$  and no longer at  $k_z = 0$ , in agreement with the analytic expression given in section II C. When twist is further increased to  $\tau_w \approx 0.33$  (not shown) a second maximum of  $Re[\sigma(k_z)]$  appears near  $k_z = 0$ . The value of  $Re[\sigma(k_z)]$  is negative at first at this secondary maximum. However, it increases with  $\tau_w$  and it is slightly positive at  $\tau_w = 0.35$  (Fig. 11c). The twisted scroll waves are then unstable for a finite range of wavevectors near  $k_z = 0$ . Increasing twist further, enlarges the range of unstable wavelengths and the instability growth rate, as shown on Fig. 11d.

Dynamical simulations reported in section IV B show that this twist-induced instability of the translation bands correspond to the "sproing" instability of ref. [10]. Before describing these results, it is worth explaining why the instability does not appear around the translation modes at  $k_z = \pm\tau_w$  but a finite wavevector away from them. This is a direct consequence of 3D rotational invariance: a twisted scroll wave the axis of which is tilted has the same frequency as one the axis of which is vertical. So, a small tilt perturbation should not change the translation mode eigenvalues  $\pm i\omega_1$  to linear order. Therefore, they remain local extrema on the translation bands, as it is observed in Fig. (12). A direct mathematical proof (based on the same reasoning) is offered in the next section.

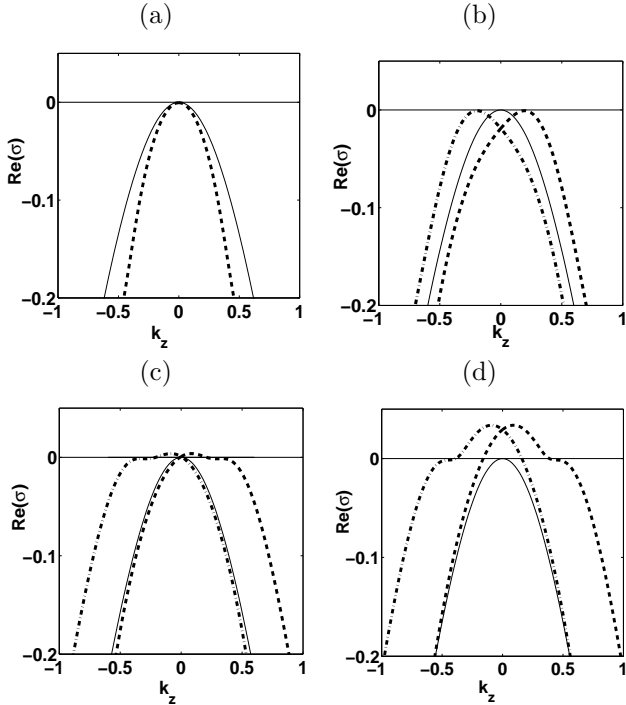


FIG. 12. Real parts of the rotation band (thin solid line) and the two translation bands (bold dashed and dash dotted lines) as a function of the wave number  $k_z$  for the same parameter values  $a = 0.8$ ,  $b = 0.01$  and  $\epsilon = 0.025$  and different values of twist : (a)  $\tau_w = 0.0$ , (b)  $\tau_w = 0.2$ , (c)  $\tau_w = 0.35$  and (d)  $\tau_w = 0.45$ . The translation bands have maxima at  $k_z = \pm\tau_w$  with a zero growth rate. A secondary maximum appears on the translation bands as the twist increases. At a threshold value of the twist it becomes unstable at a non-zero value of  $k_z$ .

Finally, we find it interesting to show in Fig. 13 the twist influence on the spectrum in the "negative line tension" parameter regime of Fig. 5, although the untwisted scroll wave is already unstable in this case. Twist modifies the spectrum in a way that is rather different from that seen in Fig. 12. It mainly amplifies the instability of the large  $k_z$  part of the spectrum .

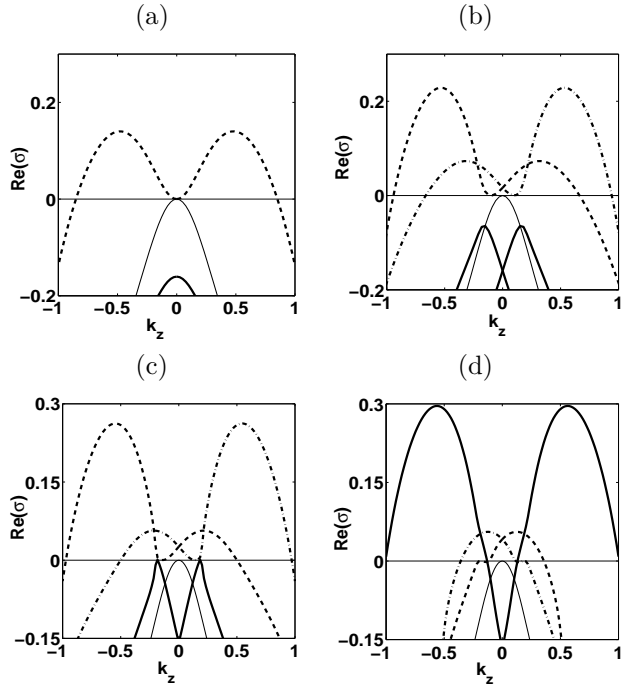


FIG. 13. Real parts of the rotation band (thin line) and the two translation bands (dashed and dashed-dotted) as a function of the wave number  $k_z$  for  $a = 0.44$ ,  $b = 0.01$  and  $\epsilon = 0.025$  and different values of twist : (a)  $\tau_w = 0.$ , (b)  $\tau_w = 0.1$ , (c)  $\tau_w = 0.14$  and (d)  $\tau_w = 0.19$ . The translation bands have a minimum zero growth rate for  $k_z = \pm\tau_w$ . The maximum growth rate of the translation bands is increased by twist. The meander modes also become less stable as twist is increased. The change in the most unstable band for  $\tau_w$  close to 0.14 appears to be due to hybridization between the translation and meander bands like the one observed in Fig. 8. The results of direct numerical simulations show that twist does not qualitatively modify the development of the zero twist instability in this regime: a "negative line tension" growth of the filament is observed.

### A. Helical destabilization and 3D rotational invariance

In order to demonstrate that the translation modes eigenvalues at  $k_z = \pm\tau_w$  remain extrema on the translation bands, we show that

$$\frac{d\sigma}{dk} \Big|_{k_z=\pm\tau_w} = 0 \quad (30)$$

We proceed in two steps. First, perturbation theory is used to compute the eigenvalues of modes close to the translation modes on the translation bands. For definiteness, we consider modes at  $k_z = -\tau_w + \delta k$ , close to the translation mode  $(u_t, v_t)$  at  $k_z = -\tau_w$  with  $\sigma = i\omega_1$ . Eq. (7, 8) can be written without approximation,

$$\sigma(k_z) \begin{pmatrix} u_1 \\ v_1 \end{pmatrix} = (-i\delta k^2 + 2\delta k\tau_w + 2i\tau_w\delta k\partial_\phi) \begin{pmatrix} u_1 \\ 0 \end{pmatrix} + \mathcal{L}_{k_z=-\tau_w} \begin{pmatrix} u_1 \\ v_1 \end{pmatrix} \quad (31)$$

Seeking in perturbation,  $u_1 = u_t + \delta u_1, v_1 = v_t + \delta v_1$ , one obtains to first order in  $\delta k$ ,

$$\delta\sigma \begin{pmatrix} u_t \\ v_t \end{pmatrix} + i\omega_1 \begin{pmatrix} \delta u_1 \\ \delta v_1 \end{pmatrix} = 2\delta k\tau_w(1 + i\partial_\phi) \begin{pmatrix} u_t \\ 0 \end{pmatrix} + \mathcal{L}_{k_z=-\tau_w} \begin{pmatrix} \delta u_1 \\ \delta v_1 \end{pmatrix} \quad (32)$$

Multiplying by the left eigenvector  $(\tilde{u}_t, \tilde{v}_t)$  of  $\mathcal{L}_{k_z=-\tau_w}$  for the eigenvalue  $i\omega_1$  and taking the scalar product gives,

$$\frac{d\sigma}{dk} \Big|_{k_z=\pm\tau_w} = \frac{2\tau_w}{\langle \tilde{u}_t, u_t \rangle + \langle \tilde{v}_t, v_t \rangle} \langle \tilde{u}_t, (1 + i\partial_\phi)u_t \rangle \quad (33)$$

Thus, the translation modes remain extrema on the translation bands, if

$$\langle \tilde{u}_t, (1 + i\partial_\phi)u_t \rangle = 0. \quad (34)$$

Eq. (34) is a consequence of 3D rotational invariance as we proceed to show. The perturbation corresponding to inclining the scroll axis can be found by expressing the inclined scroll in the vertical scroll referential, similarly to what was done to determine translation modes (Eq. (11, 12)).

One obtains,

$$\begin{pmatrix} u_{inc}^{(1)} \\ v_{inc}^{(1)} \end{pmatrix} = \exp[i(\omega_1 t + \tau_w z)] \begin{pmatrix} u_{inc} \\ v_{inc} \end{pmatrix} = \exp[i(\omega_1 t + \tau_w z)] \left[ z \exp(i\phi)(\partial_r + \frac{i}{r}\partial_\phi) + \tau_w r \exp(i\phi)\partial_\phi \right] \begin{pmatrix} u_0 \\ v_0 \end{pmatrix} \quad (35)$$

and the complex conjugate mode. One can directly check that  $u_{inc}^{(1)}, v_{inc}^{(1)}$  obey the linearized time dependent equations. Namely,

$$(\partial_t + 2\tau_w\partial_{\phi z}^2 - \partial_{zz}^2)u_{inc}^{(1)} = (\omega_1\partial_\phi + \tau_w^2\partial_{\phi\phi}^2 + \nabla_{2D}^2)u_{inc}^{(1)} + [\partial_u f(u_0, v_0)u_{inc}^{(1)} + \partial_v f(u_0, v_0)v_{inc}^{(1)}]/\epsilon \quad (36)$$

$$\partial_t v_{inc}^{(1)} = \omega_1\partial_\phi v_{inc}^{(1)} + \partial_u g(u_0, v_0)u_{inc}^{(1)} + \partial_v g(u_0, v_0)v_{inc}^{(1)} \quad (37)$$

Eq. 37 shows that  $(u_{inc}, v_{inc})$  (Eq. (35)) obey

$$[\mathcal{L}_{k_z=-\tau_w} - i\omega_1] \begin{pmatrix} u_{inc} \\ v_{inc} \end{pmatrix} = \begin{pmatrix} -i2\tau_w(1 + i\partial_\phi)u_t \\ 0 \end{pmatrix} \quad (38)$$

The inhomogeneous r.h.s. of Eq. (38) comes from the fact that the  $\partial_z$  derivative terms in Eq. (37) act both on the exponential prefactor and on the intrinsic  $z$  dependence of  $u_{inc}$  (Eq. (35)), while in effect only their action on the exponential term is taken into account in Eq. (38) (through the  $k_z$  dependence of  $\mathcal{L}_{k_z}$ ).

Eq. (38) directly gives the sought orthogonality relation (34) after multiplying both of its sides by the left eigenvector  $(\tilde{u}_t, \tilde{u}_t)$  of  $\mathcal{L}_{k_z=-\tau_w}$  with eigenvalue  $i\omega_1$  and taking the scalar product.

## B. The sproing bifurcation

In order to study the nonlinear development of the twist-induced instability shown in the parameter regime of Fig. 12c, d, we performed direct numerical simulations of twisted scroll waves using periodic boundary conditions at the top and bottom of the simulation box.

Two kinds of initial conditions were used. The simplest one consisted of two dimensional spirals stacked along the vertical ( $z$ ) axis. The twist was introduced by rotating them around this vertical axis. The main disadvantage of this type of initial conditions was that they usually are far from a stationary twisted scroll wave and from a restabilized wave when it existed. As a result, reaching the asymptotic attracting state could be very costly in computational time. In order to avoid this problem we mainly used initial conditions constructed using results of previous direct simulations on a grid with the same values of the parameters and the same horizontal size but of a different vertical extension, interpolating linearly the values of the  $u$  and  $v$  field on the new grid.

For definiteness, we describe the result for the parameters of Fig. 12.

We first focus on the case when a single turn of twist is initially imposed as in ref. [10]. This case is special for the following reasons. On one hand, the previous linear stability results (Fig. 12) show that all the potentially unstable modes correspond to  $|k_z| < \tau_w$ . On the other hand, in a box of height  $H$ , the only possible  $k_z$  values compatible with the imposed top and bottom periodic boundary conditions are multiple of  $2\pi/H$ . Therefore, for a single turn of twist  $\tau_w = 2\pi/H$ , there is a single potentially unstable mode in the simulation box and it stands at  $k_z = 0$ .

A series of dynamical simulations were performed in boxes of varying heights  $H$ . The initial twist was correspondingly varied from  $\tau_w = 0.3$  to  $\tau_w = 0.5$ .

For low values of twist, the twisted initial state simply evolves toward a straight twisted scroll wave. The instantaneous filament has an helical shape that rotates at a fixed time independent frequency around its vertical axis. In each horizontal plane, the wave is seen as a spiral steadily rotating around the helix axis.

Beyond a threshold twist  $\tau_c$ , the twisted initial state evolves toward a more complex state. The threshold twist is estimated to be  $\tau_c = 0.352$  from the direct numerical simulations. It closely corresponds to the value 0.350 obtained from the linear stability analysis for the instability of the  $k_z = 0$  modes (the instability threshold twist at  $k_z \neq 0$  is  $\tau \simeq .345$ ). The asymptotic scroll wave state is shown in Fig. 14 for  $\tau_w = 0.381$  and it is qualitatively similar for other values  $\tau_w > \tau_c$ . The instantaneous filament takes an helical shape at each time. The axis of this instantaneous helical shape is independent of time but its other characteristics vary with time. The point of the instantaneous filament in a given horizontal plane (i.e. the spiral wave tip in that plane) closely follows an epicycloidal motion (Fig. 14) and the instantaneous filament global evolution can be accurately parameterized as

$$\begin{cases} x = R_1 \cos(\omega_s t + \tau_w z + \phi) + R \cos(\omega_m t + \tau_w z) \\ y = R_1 \sin(\omega_s t + \tau_w z + \phi) + R \sin(\omega_m t + \tau_w z) \end{cases} \quad (39)$$

The pulsation  $\omega_s$  and the radius  $R_1$  are close to the pulsation and radius of the stationary straight twisted scroll. The pulsation  $\omega_m$  is found to be small compared to  $\omega_s$  (Table. II). The radius  $R$  is zero at the bifurcation threshold. It increases and become comparable to  $R_1$  as  $\tau_w$  increases past  $\tau_c$  (Fig. 15). As  $R\omega_m$  remains small compared to  $R_1\omega_s$ , the movement of the spiral tip in an horizontal plane can be described as a rapid rotation movement around a slowly moving "mean" point (Fig. 14). The bifurcation can thus be described as in ref. [10] as a transition in the shape of these slowly moving points, the "mean filament", from a straight shape to an helix of radius  $R$  (with the same axis as the instantaneous filament).

The amplitude of the sproing bifurcation can be measured by the radius  $R$  of the helical mean filament<sup>4</sup>. The numerical simulations results (Fig. 15) show that  $R$  behaves as  $\sqrt{\tau_w - \tau_c}$  confirming the normal Hopf type of the bifurcation. The motion of a filament point in an horizontal plane is quasiperiodic with two frequencies (see Eq. 39 and Fig. 14)  $\omega_m$  and  $\omega_s$ . As reported in Table II, the frequency  $\omega_m$  closely agrees with the difference  $\omega_1 - \omega_{t,k_z=0}$  between the stationary twisted scroll pulsation ( $\omega_1$ ) and the imaginary part of the unstable mode at  $k_z = 0$ , as expected from a Hopf bifurcation in a rotating frame. The other frequency  $\omega_s$  is equal to the twisted scroll pulsation  $\omega_1$  at the bifurcation point but departs from it as one moves away from it.

Some insight into the sproing bifurcation and the value of  $\omega_s$  can be gained by computing the local twist of the restabilized scroll wave. The mean filament can be taken as the central curve of a ribbon, one edge of which is the instantaneous filament of length. The local twist of this ribbon is equal to (using Eq. (C2) and (C4) of appendix C)

---

<sup>4</sup> $R$  can be easily computed as  $R = (R_{max} + R_{min})/2$  where  $R_{max}$  ( $R_{min}$ ) is the maximum (minimum) distance of the instantaneous filament from its axis in an horizontal plane ( $R_{min}$  should be counted negative value if the spiral tip trajectory encloses the axis of the helices during one rotation period).

$\tau_w$	$\omega_m$	$\omega_1(\tau_w) - Im(\sigma_t(k_z = 0))$	$\omega_1(\tau_w)$	$\omega_s$	$\tau$	$\omega_1(\tau)$
0.50	0.053	0.049	1.973	1.91	0.353	1.892
0.45	0.061	0.059	1.943	1.88	0.347	1.889
0.40	0.066	0.066	1.916	1.88	0.347	1.889
0.355	0.063	0.063	1.891	1.88	0.349	1.890

TABLE II. For different values of the imposed twist  $\tau_w$ , values of the pulsation of the restabilized mean filament  $\omega_m$ , of the difference between the pulsation of the steady scroll  $\omega_1(\tau_w)$  and the imaginary part of the unstable translation mode for  $k_z = 0$ , the pulsation of the steady scroll  $\omega_1(\tau_w)$ , the pulsation of the restabilized spiral around the mean filament  $\omega_s$  the local twist  $\tau$  of the restabilized state and the calculated corresponding pulsation  $\omega_1(\tau)$ . One notes that  $\omega_s$  is close to  $\omega_1(\tau)$

$$\tau = \frac{2\pi - Wr}{L} = \frac{\tau_w}{1 + (R\tau_w)^2} \quad (40)$$

where  $L$  is the mean filament length and  $\tau_w = 2\pi/H$  is the twist imposed on the initial straight scroll wave. Eq. 40 shows that sproing decreases the twist. Moreover, when the initial twist is increased the average helix radius  $R$  also increases so as to maintain the local twist  $\tau$  approximately constant, as shown in Fig. 15b. The frequency  $\omega_s$  appears to remain close to the frequency of twisted straight scroll wave with this value of the local twist, as shown in Table II.

It is interesting to compare the above results with what happens when the initial condition contain  $n$  turns of twist since the modes with  $k_z = j2\pi/H, j = 1, \dots, n-1$  obey both  $k_z < \tau_w$  and the periodic boundary conditions. Analyzing moderate values of the imposed twist  $\tau_w = n2\pi/H$  requires of course to extend the box height  $H$  proportionally to  $n$  and restricted us to  $n \leq 5$ .

The simplest interesting case occurs when a single unstable mode with  $k_z \neq 0$  can develop in the simulation box. The linear stability results shows that this can only happen close to the instability threshold when the instability growth rate is very low, otherwise the  $k_z = 0$  mode is also unstable. This is achieved, for instance, for  $a = 0.8$ ,  $b = 0.01$  and  $\epsilon = 0.025$  and  $n = 5$  initial turns of twist in a box of height  $H = 613 \times dx$  with  $dx = 0.15$ . The single unstable mode  $k_z = 2\pi/H = 0.069$  corresponds to a wavelength equal to the box height  $H$ . With this parameter choice, a direct simulation shows that the instability develops. The asymptotic state is similar to the previously described one for a single unstable mode at  $k_z = 0$ . The movement of the corresponding instantaneous filament can be parameterized using polar coordinates in each horizontal plane by:

$$x + iy = R_1 e^{i\omega_1 t + \tau_w z} + R_2 e^{i\omega_2 t + (\tau_w - k_{z2})z + \psi}, \quad (41)$$

where  $R_1 \simeq 0.31$  and  $\omega_1 = 1.85$  are close to the radius and pulsation of the straight twisted scroll and where  $R_2 \simeq 0.1$  and  $\omega_2 = -0.047$  are small compared to  $R_1$  and  $\omega_1$ . The wavenumber  $k_{z2} = 0.069$  is equal to the single unstable wavenumber that can develop in the simulation box. The computation of  $\omega_2$  shows that it is close of the difference  $\omega_1(\tau_w) - Im(\sigma_t(k_{z2}))$ . In contrast to the single turn of twist case, the instantaneous filament shape is slightly different from an helix since its radius varies along the vertical axis. The motion can nonetheless be interpreted in the same manner by considering that the scroll rotates uniformly around a slowly moving helical mean filament of radius  $R_2$  and pitch  $2\pi/(\tau_w - k_{z2})$ .

The case where several unstable modes of the translation band can develop in the simulation box, can only be studied in a box where several turns of twist are initially imposed. The asymptotic state reached in such a case after the instability development, starting from an initially twisted straight scroll wave is shown in Fig. 16. It is significantly more complicated than in the single unstable mode case and the instantaneous filament shape is rather different from a simple helix.

In each horizontal plane, the spiral tip rotates uniformly around a slowly moving point. The positions of these slowly moving points can be numerically computed<sup>5</sup> and used to construct the position of a mean filament. The motion of the mean filament is found to be well parameterized in each horizontal plane by

<sup>5</sup>This can be done by considering the mean filament as the mean position of the instantaneous filament over a rotation period, or by considering it as the instantaneous center of rotation of the instantaneous filament in a plane or by removing the high frequency peak in the Fourier spectrum of the instantaneous filament motion. These three methods give very similar results.

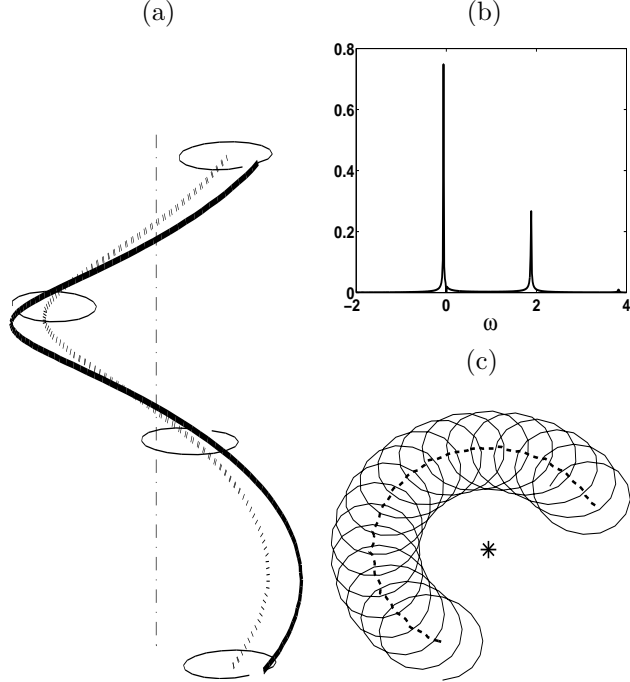


FIG. 14. (a): the bold solid line represents the helical instantaneous filament, the dotted line the mean filament and the thin solid lines the quasi-circular trajectories of the instantaneous filament in horizontal planes of equally spaced  $z$ . Parameters values are  $a = 0.8$ ,  $b = 0.01$  and  $\epsilon = 0.025$ , the simulation box is  $(128 \times 128) \times 110$  with  $dx = 0.15$ , corresponding to  $\tau_w = 0.381$ . (b): Modulus of the Fourier transform of the spiral tip complex position  $(x + iy)$  in an horizontal plane for the same parameter regime. The peak at  $\omega \approx -0.064$  corresponds to the slow movement of the mean filament in the plane while the peak at  $\omega = 1.884$  corresponds to the rapid rotating motion of the spiral. The Fourier transform was performed using 2048 points with a time spacing of  $\delta t = 0.1969$ . (c): the thin solid line is the trajectory of the spiral tip in an horizontal plane and the bold dashed line is the trajectory of the mean filament in that plane. The mean filament rotates clockwise while the fast rotation of the spiral tip is counterclockwise. At a given time, the projection of the mean filament and instantaneous filaments on the horizontal plane are circles centered on the helices axis position marked by a star.

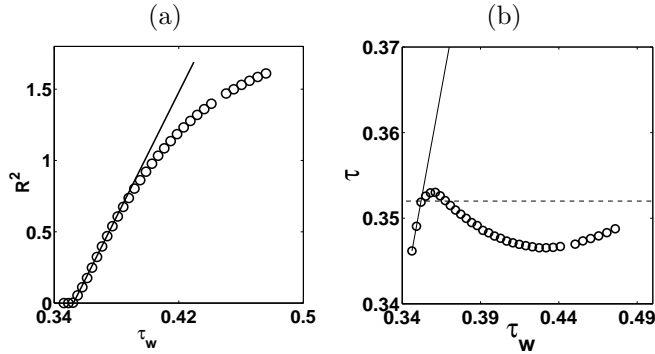


FIG. 15. (a) (○) Radius ( $R$ ) of the helical mean filament as a function of the twist  $\tau_w$ , for a stationary straight twisted scroll wave and linear interpolation of  $R^2$  for small values of  $\tau_w - \tau_c$  (thin continuous line) where the computed threshold twist is  $\tau_c = 0.352$ . The parameters are  $a = 0.8$   $b = 0.01$   $\epsilon = 0.025$ . (b): local twist of the restabilized filament as a function of  $\tau_w$ . The dashed line is the line of equation  $\tau = \tau_c$ , the continuous line is the line of equation  $\tau = \tau_w$ .

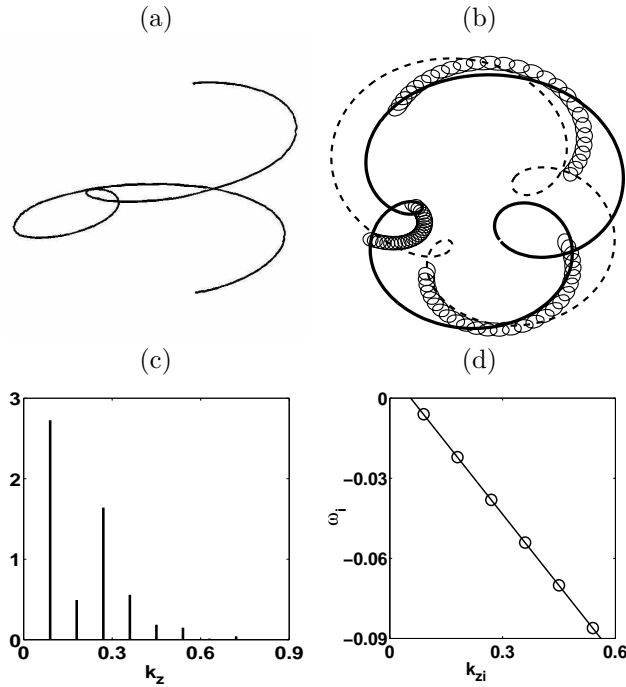


FIG. 16.  $a = 0.8$ ,  $b = 0.1$ ,  $\epsilon = 0.025$ , the simulation box size is  $(128 \times 128) \times 349$ , the space step is  $dx = 0.2$  and five turns of twist are imposed, which corresponds to  $\tau_w = 0.450$  (a): The bold solid line represents the restabilized mean filament. The instantaneous filament and the quasi circular trajectories of instantaneous filaments in horizontal planes are not shown. (b): The dashed and solid bold lines represent a top view of the instantaneous filament at two given times. The three thin solid lines are typical trajectories of the spiral tip in horizontal planes. The motion of the spiral tip in each plane is the composition of a fast counterclockwise and a slow clockwise rotations. (c): Modulus of the space Fourier transform of the complex mean filament position  $(x(z) + iy(z))$ . The amplitude of each mode is constant in time while its phase grows linearly in time with a constant pulsation  $\omega(k_z)$  shown in (d). For the Fourier modes with an amplitude significantly different from zero,  $\omega(k_z)$  is a linear function of  $k_z$ .

$$x + iy = \sum_{j=1 \dots n} R_j e^{i(k_z^{(j)} z + \omega_j t + \phi_j)} \quad (42)$$

where  $z$  denotes the vertical position of the plane and  $k_z^{(j)}$  are the wavenumbers of the modes that have developed in the simulation box. All the observed  $k_z^{(j)}$  have the same sign as  $\tau_w$ . As seen from Eq. 42, the corresponding modes have an amplitude  $R_j$  which is constant in time and a phase  $\omega_j t + \phi_j$  which evolves linearly in time. Moreover, the pulsations  $\omega_j$  are linearly related to the  $k_z^{(j)}$ ,  $\omega_j = \omega + k_z^{(j)} c$ , as shown in Fig. 16. Thus, the mean filament parameterization can be rewritten as

$$x + iy = e^{i\omega t} F(z - ct) \text{ with } F(z) = \sum_{j=1 \dots n} R_j e^{i(k_z^{(j)} z)} \quad (43)$$

This explicitly shows that the mean filament deformation propagates as a nonlinear wave of constant shape in the vertical direction. It was indeed directly checked that the mean filament shape did not noticeably change at long times in our simulation (i.e. for time intervals as long as  $\Delta t = 2000$ ). A direct computation of the twist shows that it is almost uniform and that its mean value is significantly lower than the one obtained when only  $k_z = 0$  mode can grow. In the case depicted in Fig. 16, the mean local twist of the restabilized state is 0.327 whereas in the restabilized state when only the  $k_z = 0$  mode can be destabilized, the mean local twist is equal to 0.347.

The stability of the simple restabilized helices was tested in the parameter regime were the more complex state of Fig. 16 existed. To this end, a simulation was first performed with a single turn of twist in a box height chosen such that the initial twist was equal to  $\tau_w = 0.45$ . It produced, as already described, a restabilized helix similar to the one shown in Fig. 14. Five copies of this restabilized helix were then vertically stacked. The resulting five turn helix was used as the initial condition for a simulation analogous to the one shown in Fig. 16. It was observed to evolve toward a complex state identical to the one shown in Fig. 16. This clearly shows that the simple helices are unstable and strongly suggest that the complex state of Fig. 16 is the unique attractor in this parameter regime. We repeated this computation with an initial twist of 0.357 and again a similar complex state was produced.

Systematically varying the initial twist would permit to see whether these complex states directly appear at the instability threshold or arise from a secondary bifurcation of stable simple helical states. More generally, further studying the filament shapes in longer boxes with more unstable modes would be quite instructive. Both tasks require more computer time and power than presently available to us and should be left for other studies.

## V. CONCLUSION

We have searched to gain and present a general view of scroll wave linear instabilities and of their nonlinear developments for a simple model of an isotropic excitable medium. Different types of instabilities have been shown to arise depending upon the band of modes to which they belong. These different instabilities have been found to develop along different ways and to give rise to distinctly different restabilized states that we have endeavored to characterize.

The negative line tension type of instability has been found to occur in the weakly excitable part of the phase diagram and to be strictly linked to 2D spiral drift in an external field. In this respect, it seems worth to try and better analyze the mechanisms of spiral drift change. The meandering instability is present in 3D in a larger parameter region than in 2D. On the "small core" side of the phase diagram, scroll wave meander in a regime where spirals are steadily rotating, as previously noted [15]. The long wavelength deformation of the meander band is however not directly related to spiral drift. The introduction of twist has been found to induce a deformation of the translation bands. Above a threshold twist, this gives rise to the sproing instability which takes place a finite wavevector away from the translation mode. This has been shown to be a general consequence of 3D rotational invariance and it explains that the sproing bifurcation is not captured by small twist approaches. The bifurcated state arising from the growth of a single unstable mode has been found to take a simple helical shape as previously described [10]. However, a more complex filament deformation has been observed to result from the growth of several unstable modes. Simulations in larger boxes appear needed to better analyze these states.

The present study appears worth extending along several other lines. It certainly is important to investigate how the present results extend to more realistic models of excitable media, specially in the cardiac physiology context. It will also be quite interesting to see how rotating anisotropy [30–33], or spatially varying properties induce the different instabilities or interact with them. Deeper insights into the behavior of these complex waves in various situations may be gained by developing and analyzing of reduced models reproducing the basic phenomenology here uncovered. We hope to be able to report progress in this direction soon. Advances in 3D visualization [9,34] appear to render

possible detailed experimental characterization of scroll wave instabilities and dynamics. We hope that the present results will also be seen as a further motivation to undertaking this challenging task.

## APPENDIX A: NUMERICAL METHODS

### 1. Determination of the steady state

Determining the stationary scroll waves consists in solving the nonlinear eigenvalue problem (6). To this end, the equations are first discretized on a polar grid of size  $(N_r \times N_\phi)$ . This provides a set of  $2(N_r \times N_\phi)$  equations (the values

of the r.h.s of (6) on the grid points) with  $2(N_r \times N_\phi) + 1$  unknowns (the values of the field  $u_0$ ,  $v_0$  on the points of the grid and the pulsation  $\omega$ ). This indetermination comes from the rotational invariance of the problem and can be taken care of by setting the value of  $u_o(N_r, N_\phi)$  to 0.5. One thus has to find the zeros of  $2(N_r \times N_\phi)$  non linear equations of  $2(N_r \times N_\phi)$  variables.

This can be done accurately using Newton's method. The linear operator involved in Newton's method is inverted using an iterative technique (biconjugate gradient [35]) and the starting point is either the result of a direct numerical simulation interpolated on the polar grid or the result of a previous computation with slightly different parameters. We found that the Newton's method always converged and that the convergence was exponential and allowed to reach accuracies of order  $10^{-8}$  in  $L_2$  norm<sup>6</sup> in a few steps (about 10 which take about an hour using a DEC alpha PWS 500 Workstation for a grid of  $80 \times 160$  points) whereas direct numerical simulations allowed only an accuracy of order unity in  $L_2$  norm.

### 2. Computation of the linear stability spectrum

The eigenvectors of  $\mathcal{L}_{k_z}$  are denoted by  $e_1, e_2, \dots$  and indexed according to the real part of the corresponding eigenvalues  $\sigma_1 \geq \sigma_2 \geq \dots$ . In order to accurately compute the eigenvalues of  $\mathcal{L}_{k_z}$  of largest real parts, we have used an iterative method proposed and analyzed in [20]. It is briefly described in this appendix and some details of our implementation are provided.

The idea of the algorithm is to diagonalize a projection of  $\mathcal{L}_{k_z}$  in a subspace (approximately) spanned by the eigenvectors  $e_1, \dots, e_m$  corresponding to a given number  $m$  of eigenvalues of largest real parts.

The algorithm proceeds in three main steps.

The first step consists in creating an appropriate vector  $x_1$  for generating the diagonalization subspace. A suitable choice is to take  $x_1 = \exp(\mathcal{L}_{k_z} t)x_0$  for a generic vector  $x_0$ . This suppresses the components of  $x_1$  on the eigenvectors on high index [note that these eigenvectors correspond to eigenvalues of large modulus]. The end consequence is that truncation at level  $m$  produces an error of order  $\exp[t(Re(\sigma_{m+1} - \sigma_i))]$  on the representation of the  $i$ -th eigenvector (for  $i < m$ ) [20]. In practice, multiplication by the exponential is approximately achieved by computing by iterations  $x_1 = (1 + dt\mathcal{L}_{k_z})^{t_0/dt}x_0$ , for an arbitrary vector  $x_0$ , a sufficiently large integer  $t_0/dt$  and a sufficiently small  $dt$  to prevent the time stepping scheme from being unstable (this means that  $dt$  is lower than  $1/\max(\|\lambda_i\|)$ , here  $dt \simeq 10^{-5}$ ).

The second step consists in generating an appropriate subspace  $E$  for diagonalization. This is taken to be the space  $E$  spanned by  $(G(\mathcal{L}_{k_z}))^n x_1$ ,  $n = 0 \dots m - 1$  where  $G$  is an polynomial, the choice of which is discussed below. Explicitly, the computation of an orthonormal base of  $E$  and of the matrix  $A = a_{i,j}$  of the projection of  $(G(\mathcal{L}))_m$  on  $E$  proceeds recursively as follows. Let  $x_1, \dots, x_n$  be the  $n$  first element of the base of  $E$  and  $G(\mathcal{L}_{k_z})x_n = y_n$ . Then, at the next step we compute:

$$x_{n+1} = \frac{y_n - \sum_{i=1 \dots n} (y_n \cdot x_i) x_i}{\|y_n - \sum_{i=1 \dots n} (y_n \cdot x_i) x_i\|_2}. \quad (\text{A1})$$

The construction ends at step  $m$ . This building of an orthonormalized base of  $E$  presents the advantage of decreasing the contribution of the first eigenmodes in the elements of higher order of the base. Otherwise, this contribution would be dominant and would result in a lower accuracy in the computation. In our case, the scalar product is defined by a discretized version of the standard scalar product (15):

---

<sup>6</sup>We define  $\|u, v\|_2 = \sum(u_{i,j}^2 + v_{i,j}^2)$

$$(x_i, y_j) = \sum_{i_r} \sum_{i_\theta} x_i(i_r, i_\theta) y_j(i_r, i_\theta) i_r dr d\theta dr \quad (A2)$$

The third step consists in the diagonalization of an appropriate truncation of  $(G(\mathcal{L}_{k_z}))$ . Since  $E$  is not invariant under the application of  $(G(\mathcal{L}_{k_z}))$ , the orthogonal projection  $G_m$  of  $G(\mathcal{L}_{k_z})$  onto  $E$  is considered. Its matrix elements are:

$$g_{i,j} = (x_i, y_j), \quad (i, j) \in \{1 \dots m\} \times \{1 \dots m\} \quad (A3)$$

The obtained matrix is diagonalized and both its eigenvectors and its eigenvalues are computed. It is checked at the end that the leading eigenvectors of  $G_m$  are good approximations of the leading eigenvectors of  $\mathcal{L}_{k_z}$ .

The choice of the polynomial  $G$  is of some importance. Indeed, the simplest and computationally most efficient choice would be to take  $G(X) = X$ . This would result in the amplification of the contribution of the eigenmodes of  $\mathcal{L}_{k_z}$  of large index [i.e corresponding to eigenvalues of large modulus] and,  $\mathcal{L}_{k_z}$  being ill-conditioned, would prevent the success of the method. We have used  $G(X) = (1 + dtX)^{t_1/dt}$ , with  $t_1$  chosen large enough to make  $G(\mathcal{L}_{k_z})$  differ significantly from the identity (a typical value was  $t_1 = 0.5$ ). Despite the increase in computational cost, this choice significantly increases the accuracy of the method by decreasing the contribution of the eigenmodes of negative eigenvalues. Using  $m = 50$ , the 10 most unstable eigenmodes and eigenvalues are obtained with a good accuracy:  $\|(\sigma - \mathcal{L}_{k_z})(u_1, v_1)\|_2 < 10^{-6}$ .

### 3. Direct numerical simulations

Direct numerical simulations of three dimensional excitable media were performed using a forward Euler explicit timestepping scheme. The diffusion operator was evaluated using finite differences and a 19 points formula [36],

$$\begin{aligned} 6dx^2 \delta u_{i,j,k} = & -24u_{i,j,k} \\ & + 2(u_{i+1,j,k} + u_{i-1,j,k} + u_{i,j+1,k} + u_{i,j-1,k} + u_{i,j,k+1} + u_{i,j,k-1}) \\ & + u_{i+1,j+1,k} + u_{i+1,j-1,k} + u_{i+1,j,k+1} + u_{i+1,j,k-1} \\ & + u_{i-1,j+1,k} + u_{i-1,j-1,k} + u_{i-1,j,k+1} + u_{i-1,j,k-1} \\ & + u_{i,j+1,k+1} + u_{i,j+1,k-1} + u_{i,j-1,k+1} + u_{i,j-1,k-1} \end{aligned} \quad (A4)$$

This method has two main advantages compared with the classical 7 points formula. First its stability limit allows greater time steps and therefore the computing time in spite of the additional operations involved in the Laplacian evaluation is found to be 1.3 times smaller. Second, the error made when evaluating the diffusion operator is isotropic at the dominant order (order  $dx^2$ ), whereas with the 7 points formula it depends of the grid orientation.

No-flux boundary conditions  $\vec{n} \cdot \vec{\nabla} u = 0$  are imposed on the vertical sides of the box and either no-flux or periodic boundary conditions are chosen on the top and bottom boundaries.

The position of the instantaneous filament in the horizontal planes is computed as the intersection of a  $u = 0.5$  and a  $v = 0.75$  ( $0.5a - b$ ) isosurfaces.

### APPENDIX B: SPIRAL DRIFT IN AN EXTERNAL FIELD

In the presence of a small external field  $E$ , the spiral rotation center drifts at a constant velocity proportional to the field magnitude but at an angle with the field direction [37–39] as given by Eq. (18) of the main text. The drift coefficients  $\alpha_{\parallel}$  and  $\alpha_{\perp}$  have been computed in the free boundary limit ( $\epsilon \ll 1$ ) both for small core [23] and large core spirals [14]. We derive here a general formula (Eq. (B10) below) for the drift coefficient  $\alpha = \alpha_{\parallel} + i\alpha_{\perp}$  as a matrix element between the translation eigenvector  $(u_t, v_t)$  of  $\mathcal{L}$  and the corresponding right eigenvector  $(\tilde{u}_t, \tilde{v}_t)$  of  $\mathcal{L}$ .

With an added external field  $E$ , Eq. (1, 2) read

$$\partial_t u = \nabla^2 u + f(u, v)/\epsilon - E \cdot \nabla u, \quad (B1)$$

$$\partial_t v = g(u, v). \quad (B2)$$

We choose a coordinate system with the  $x$ -axis along the field direction and corresponding polar coordinates  $(r, \theta)$ . We analyze the motion of a counterclockwise rotating spiral which is stationary, for  $E = 0$ , in the rotating referential  $(r, \phi)$  with  $\phi = \theta - \omega_1 t$ . Since  $\partial_x = \cos(\theta)\partial_r - \sin(\theta)/r\partial_\theta$ , the field term  $E \cdot \nabla u$  can be written in the rotating referential

a	r.h.s of Eq. (B10)	$\alpha_{\parallel} - i\alpha_{\perp}$
0.44	-2.05 -0.78i	-1.97-0.84i
0.62	3.5 - 0.47i	3.4 -0.42i
0.7	1.59 - 0.80i	1.62 -0.83i

TABLE III. For  $b = 0.01$ ,  $\epsilon = 0.025$  and several values of  $a$ , the drift coefficients given by Eq. (B10) computed using the eigenmodes of  $\mathcal{L}_{k_z}$  and of its adjoint and the drift coefficients  $\alpha_{\parallel} - i\alpha_{\perp}$  measured in direct numerical simulations.

$$\begin{aligned} -E\partial_x u &= -E[\cos(\phi + \omega_1 t)\partial_r u - \sin(\phi + \omega_1 t)/r\partial_{\phi} u], \\ &= -E/2[\exp(i\omega_1 t)\exp(i\phi)(\partial_r u + i\partial_{\phi} u/r) + c.c.]. \end{aligned} \quad (B3)$$

As will be seen below, secular terms appear when the  $E$  term on the r.h.s. of Eq. (B1) is treated in perturbation. Their origin is, of course, the induced spiral drift. Anticipating this phenomenon, we suppose that the spiral rotates steadily in the frame with coordinates  $(r, \theta)$  which drifts with respect to the lab frame with coordinates  $(x, y)$ . That is,

$$x = x_0(t) + r \cos(\phi + \omega_1 t), \quad (B4)$$

$$y = y_0(t) + r \sin(\phi + \omega_1 t), \quad (B5)$$

and

$$\partial_t|_{r,\phi} = \partial_t|_{x,y} + \omega_1 \partial_{\phi} + \dot{x}_0 \partial_x + \dot{y}_0 \partial_y. \quad (B6)$$

The supplementary terms proportional to  $\dot{x}_0$  and  $\dot{y}_0$  should be chosen to cancel the unwanted secular terms. This determines the spiral drift. Explicitly, we rewrite Eq. (B6) using the rotating coordinates as

$$\partial_t|_{x,y} = \partial_t|_{r,\phi} - \omega_1 \partial_{\phi} - 1/2[(\dot{x}_0 - i\dot{y}_0)\exp(i\omega_1 t)\exp(i\phi)(\partial_r + i\partial_{\phi}/r) + c.c.]. \quad (B7)$$

Substitution of this formula in Eq. (B1,B2) and linearization under the form  $u = u_0(r, \phi) + u_p \exp(i\omega_1 t) + c.c.$ ,  $v = v_0(r, \phi) + v_p \exp(i\omega_1 t) + c.c.$  gives,

$$(i\omega_1 - \mathcal{L}) \begin{pmatrix} u_p \\ v_p \end{pmatrix} - 1/2(\dot{x}_0 - i\dot{y}_0) \begin{pmatrix} u_t \\ v_t \end{pmatrix} = -E/2 \begin{pmatrix} u_t \\ 0 \end{pmatrix} \quad (B8)$$

Multiplying by the left eigenvector  $\mathcal{L}$  of eigenvalue  $i\omega_1$  would show the need for secular terms if we had not introduced the drift terms. Here, however it simply determines the drift as

$$\dot{x}_0 - i\dot{y}_0 = E \frac{\langle \tilde{u}_t, u_t \rangle}{\langle \tilde{u}_t, u_t \rangle + \langle \tilde{v}_t, v_t \rangle} \quad (B9)$$

Equivalently, this gives the sought formula for the drift coefficients

$$\alpha_{\parallel} - i\alpha_{\perp} = \frac{\langle \tilde{u}_t, u_t \rangle}{\langle \tilde{u}_t, u_t \rangle + \langle \tilde{v}_t, v_t \rangle} \quad (B10)$$

### APPENDIX C: TWIST AND WRITHE OF A RIBBON

We recall the definition of quantities associated to closed ribbons and some useful mathematical properties for analyzing the “sproing” bifurcation. In particular we give a mathematical definition of the twist and its value in the case of a uniformly twisted ribbon with an helical central curve.

The local twist of a ribbon is classically defined as ([26])

$$\tau = \left( \frac{d}{ds} (\vec{p}) \wedge \vec{p} \right) \cdot \vec{t} \quad (C1)$$

where  $\vec{t}$  is the unit tangent vector to the mean curve of the ribbon,  $s$  is the curvilinear coordinate along the mean curve and  $\vec{p}$ , the unit vector perpendicular to that curve that directs the line intersecting one of the edges of the ribbon. The twist measures the spatial rotation rate of the edges of the ribbon around the mean curve.

For a closed ribbon, the linking number  $L_k$  is the integer which measures the entanglement of the two edges of the ribbon.  $L_k$  is a topological invariant which is constant under a continuous deformation of the ribbon (as long as it does not intersect itself).

The linking number is related to the integral of twist by a formula [40] (which has been popularized by its use in a molecular biology context)

$$L_k = W_r + \frac{1}{2\pi} \int_s \tau ds \quad (C2)$$

The writhing number  $W_r$  depends only of the mean curve  $\vec{r}(s)$  of the ribbon and is equal to:

$$W_r = \frac{1}{4\pi} \int ds \int ds' \frac{\partial_s \vec{r}(s) \wedge \partial_s \vec{r}(s') \cdot [\vec{r}(s) - \vec{r}(s')]}{\|\vec{r} - \vec{r}'\|^3} \quad (C3)$$

The tangent vector to  $r(s)$  traces a closed curve on the unit sphere as  $r(s)$  goes around the ribbon. The writhing number is also equal, up to an even integer, to the area enclosed on the unit sphere by this closed curve divided by  $2\pi$  [41].

An example of interest is the writhing number of a single turn of an helix of radius  $R$  and pitch  $H$  (linking the two free ends by a non self intersecting planar curve to obtain a closed curve). The tangent vectors curve encloses a spherical cap on the unit sphere of normalized area equal to  $(1 - \cos \theta)$  where  $\theta$  is the angle made by the tangent vector with the vertical axis. This gives the writhing number (up to an even integer which is seen to be zero by using the continuity of  $Wr$  and the fact that the writhing number of a straight line is equal to zero),

$$Wr = 1 - \frac{1}{\sqrt{1 + (2\pi R/H)^2}} \quad (C4)$$

#### APPENDIX D: LINK WITH AVERAGED EQUATION

In ref. [16], equations were derived for the motion of the mean scroll filament and the evolution of twist for a weakly twisted and weakly curved scroll wave. It was subsequently noted [12] that many coefficients in ref. [16] original equations were identically zero and that only four non-trivial ones remained to be determined. This approach has recently been extended to take into account fiber rotation anisotropy [33].

In this appendix, we find it of some interest to explicitly relate the averaged equations of ref. [16,12] to the computations that are performed in the main part of the present paper. One coefficient in the equations of ref. [16,12] is given by the quadratic scroll rotation frequency dependence at small twist (Eq. (29)). Unsurprisingly, the three other ones are given by the curvature of the rotation and translation bands around the corresponding symmetry eigenvalues. This explicitly confirms that the sproing instability cannot be captured in the limit considered to derive the averaged equations since the instability takes place a finite distance away from the translation symmetry eigenvalues on the translation bands.

We provide a simple-minded derivation of the equations ref. [16,12] using a Cartesian frame instead of the more sophisticated intrinsic mean filament coordinates used in ref. [16]. This limits us to consider a weakly inclined filament but we can proceed very similarly to the derivation of spiral drift in appendix B and the extension to non-isotropic or non-homogeneous medium is straightforward (but not considered here).

We denote the fixed Cartesian coordinates by  $(x, y, z)$  and by  $(r, \phi, z)$  the cylindrical coordinates of a frame rotating at the 2D spiral frequency and centered on the mean filament position  $(x_0(t, z), y_0(t, z))$ ,

$$x = x_0(t, z) + r \cos[\phi + \omega_1 t + \psi(t, z)] \quad (D1)$$

$$y = y_0(t, z) + r \sin[\phi + \omega_1 t + \psi(t, z)] \quad (D2)$$

The corresponding relations between the time and vertical ( $z$ ) derivatives in the two referentials are thus,

$$\partial_t|_{r,\phi} = \partial_t|_{x,y} + \omega_1 \partial_\phi + \partial_t \psi \partial_\phi + \partial_t x_0 \partial_x + \partial_t y_0 \partial_y \quad (D3)$$

$$\partial_z|_{r,\phi} = \partial_z|_{x,y} + \partial_z \psi \partial_\phi + \partial_z x_0 \partial_x + \partial_z y_0 \partial_y \quad (D4)$$

These relations can be rewritten using  $\partial_x + i\partial_y = \exp[i\phi + i\omega_1 t + i\psi(z, t)][\partial_r + i\partial_\phi/r]$  and introducing  $w_0 = x_0 - iy_0$ ,

$$\partial_t|_{x,y} = \partial_t|_{r,\phi} - \omega_1 \partial_\phi - \partial_t \psi \partial_\phi - \frac{1}{2} [\partial_t w_0 e^{i\phi+i\omega_1 t+i\psi} (\partial_r + i\partial_\phi/r) + c.c.] \quad (D5)$$

$$\partial_z|_{x,y} = \partial_z|_{r,\phi} - \partial_z \psi \partial_\phi - \frac{1}{2} [\partial_z w_0 e^{i\phi+i\omega_1 t+i\psi} (\partial_r + i\partial_\phi/r) + c.c.] \quad (D6)$$

$$\begin{aligned} \partial_{zz}^2|_{x,y} = & \partial_{zz}^2|_{r,\phi} + (\partial_z \psi)^2 \partial_{\phi\phi}^2 - 2\partial_z \psi \partial_{\phi z}^2 - [\partial_z w_0 e^{i\phi+i\omega_1 t+i\psi} (\partial_{rz}^2 + i\partial_{\phi z}^2/r) + c.c.] \\ & + \frac{1}{4} [(\partial_z w_0)^2 e^{2(i\omega_1 t+i\psi)} (e^{i\phi} (\partial_r + i\partial_\phi/r))^2 + c.c.] \\ & + \frac{1}{2} |\partial_z w_0|^2 \nabla_{2D}^2 - \frac{1}{2} [\partial_{zz}^2 w_0 e^{i\phi+i\omega_1 t+i\psi} (\partial_r + i\partial_\phi/r) + c.c.] \\ & - \partial_{zz}^2 \psi \partial_\phi + \partial_z \psi [\partial_z w_0 e^{i\phi+i\omega_1 t+i\psi} (\partial_{r\phi}^2 + i\partial_{\phi\phi}^2) + c.c.] \end{aligned} \quad (D7)$$

With Eq. (D5, D7), the governing reaction-diffusion equations (1,2) become

$$\begin{aligned} (\partial_t - \omega_1 \partial_\phi - \nabla_{2D}^2) u - f(u, v)/\epsilon = & \partial_t \psi \partial_\phi u + \frac{1}{2} [\partial_t w_0 e^{i\phi+i\omega_1 t+i\psi} (\partial_r u + i\partial_\phi u/r) + c.c.] + \partial_{zz}^2 u \\ & + (\partial_z \psi)^2 \partial_{\phi\phi}^2 u - 2\partial_z \psi \partial_{\phi z}^2 u - [\partial_z w_0 e^{i\phi+i\omega_1 t+i\psi} (\partial_{rz}^2 u + i\partial_{\phi z}^2 u/r) + c.c.] \\ & + \frac{1}{4} [(\partial_z w_0)^2 e^{2(i\omega_1 t+i\psi)} (e^{i\phi} (\partial_r + i\partial_\phi/r))^2 u + c.c.] \\ & + \frac{1}{2} |\partial_z w_0|^2 \nabla_{2D}^2 u - \frac{1}{2} [\partial_{zz}^2 w_0 e^{i\phi+i\omega_1 t+i\psi} (\partial_r u + i\partial_\phi u/r) + c.c.] \\ & - \partial_{zz}^2 \psi \partial_\phi u + \partial_z \psi [\partial_z w_0 e^{i\phi+i\omega_1 t+i\psi} (\partial_{r\phi}^2 u + i\partial_{\phi\phi}^2 u/r) + c.c.] \end{aligned} \quad (D8)$$

$$(\partial_t - \omega_1 \partial_\phi) v - g(u, v) = \partial_t \psi \partial_\phi v + \frac{1}{2} [\partial_t w_0 e^{i\phi+i\omega_1 t+i\psi} (\partial_r v + i\partial_\phi v/r) + c.c.] \quad (D9)$$

For a weakly curved and weakly twisted scroll wave, the r.h.s. of Eq. (D8,D9) can be treated in perturbation starting from the 2D spiral fields  $(u_0, v_0)$ . At first order, the inhomogeneous r.h.s are a superposition of time independent terms and of terms oscillating at frequencies  $\omega_1$  and  $2\omega_1$ . One can therefore seek  $(u, v)$  in perturbation as

$$\begin{pmatrix} u \\ v \end{pmatrix} = \begin{pmatrix} u_0 \\ v_0 \end{pmatrix} + \left[ \begin{pmatrix} u_1^{(2\omega_1)} \\ v_1^{(2\omega_1)} \end{pmatrix} e^{2i\omega_1 t+2i\psi} + c.c. \right] + \left[ \begin{pmatrix} u_1^{(\omega_1)} \\ v_1^{(\omega_1)} \end{pmatrix} e^{i\omega_1 t+i\psi} + c.c. \right] + \begin{pmatrix} u_1^{(0)} \\ v_1^{(0)} \end{pmatrix} \quad (D10)$$

where  $(u_1^{(2\omega_1)}, v_1^{(2\omega_1)}, u_1^{(\omega_1)}, v_1^{(\omega_1)}$  and  $(u_1^{(0)}, v_1^{(0)})$  are time-independent functions characterizing the three different first order perturbative corrections.

The  $2\omega_1$ -functions obey

$$(i2\omega_1 - \mathcal{L}) \begin{pmatrix} u_1^{(2\omega_1)} \\ v_1^{(2\omega_1)} \end{pmatrix} = \frac{1}{4} (\partial_z w_0)^2 \begin{pmatrix} (e^{i\phi} (\partial_r + i\partial_\phi/r))^2 u \\ 0 \end{pmatrix} \quad (D11)$$

The operator  $(i2\omega_1 - \mathcal{L})$  is invertible and the  $2\omega_1$  functions  $(u_1^{(2\omega_1)}, v_1^{(2\omega_1)})$  can be determined. They simply describe the inclined circular core which is viewed as elliptical in the chosen  $xy$  coordinates (these terms are absent in the filament coordinates used in ref. [16] where in effect  $\partial_z w_0$  is zero).

On the contrary, the  $\omega_1$  and constant functions arise from resonant forcing and can only be determined when solvability conditions are verified.

The  $\omega_1$  functions obey,

$$(i\omega_1 - \mathcal{L}) \begin{pmatrix} u_1^{(\omega_1)} \\ v_1^{(\omega_1)} \end{pmatrix} = \frac{1}{2} \partial_t w_0 \begin{pmatrix} u_t \\ v_t \end{pmatrix} - \frac{1}{2} \partial_{zz}^2 w_0 \begin{pmatrix} u_t \\ 0 \end{pmatrix} + \partial_z \psi \partial_z w_0 \begin{pmatrix} e^{i\phi} (\partial_{r\phi}^2 u_0 + i\partial_{\phi\phi}^2 u_0/r) \\ 0 \end{pmatrix} \quad (D12)$$

Since  $(u_t, v_t)$  is an eigenvector of  $\mathcal{L}$  with eigenvalue  $i\omega_1$ , Eq. (D12) is solvable only if its r.h.s has no component on this eigenvector. More explicitly, one obtains by multiplying Eq. (D12) by the associated left eigenvector,

$$\partial_t w_0 - \partial_{zz}^2 w_0 \frac{\langle \tilde{u}_t, u_t \rangle}{\langle \tilde{u}_t, u_t \rangle + \langle \tilde{v}_t, v_t \rangle} + \partial_z \psi \partial_z w_0 \frac{\langle \tilde{u}_t, e^{i\phi} (\partial_{r\phi}^2 u_0 + i\partial_{\phi\phi}^2 u_0/r) \rangle}{\langle \tilde{u}_t, u_t \rangle + \langle \tilde{v}_t, v_t \rangle} = 0 \quad (D13)$$

The last term on the l.h.s should vanish by rotational invariance since simply inclining a twisted scroll cannot induce its drift. This explicitly follows from Eq. (34) since

$$\langle \tilde{u}_t, e^{i\phi}(\partial_{r\phi}^2 u_0 + i\partial_{\phi\phi}^2 u_0/r) \rangle = \langle \tilde{u}_t, (1 + i\partial_\phi)u_t \rangle = 0. \quad (\text{D14})$$

Eq. (D13) [without the last term] is the equation of motion for the mean filament obtained in ref. [16,12]. In the limit considered, the mean filament motion is independent of the scroll twist and only depends on the filament curvature ( $\partial_{zz}^2 w_0$ ) with a coefficient which gives both the small  $k_z^2$  dependence of the translation bands (Eq. (23)) and spiral drift in an external field (Eq. (B10)).

The time independent component  $(u_1^{(0)}, v_1^{(0)})$  of the first 0 correction (D10) obey

$$-\mathcal{L} \begin{pmatrix} u_1^{(0)} \\ v_1^{(0)} \end{pmatrix} = \partial_t \psi \begin{pmatrix} \partial_\phi u_0 \\ \partial_\phi v_0 \end{pmatrix} - \partial_{zz}^2 \psi \begin{pmatrix} \partial_\phi u_0 \\ 0 \end{pmatrix} + (\partial_z \psi)^2 \begin{pmatrix} \partial_{\phi\phi}^2 u_0 \\ 0 \end{pmatrix} + \frac{1}{2} |\partial_z w_0|^2 \begin{pmatrix} \nabla_{2D}^2 u_0 \\ 0 \end{pmatrix} \quad (\text{D15})$$

Again since the rotation mode is an eigenvector with eigenvalue zero of  $\mathcal{L}$ , this equation can be solved only if

$$\partial_t \psi - \partial_{zz}^2 \psi \frac{\langle \tilde{u}_\phi, u_\phi \rangle}{\langle \tilde{u}_\phi, u_\phi \rangle + \langle \tilde{v}_\phi, v_\phi \rangle} + (\partial_z \psi)^2 \frac{\langle \tilde{u}_\phi, \partial_{\phi\phi}^2 u_0 \rangle}{\langle \tilde{u}_\phi, u_\phi \rangle + \langle \tilde{v}_\phi, v_\phi \rangle} + \frac{1}{2} |\partial_z w_0|^2 \frac{\langle \tilde{u}_\phi, \nabla_{2D}^2 u_0 \rangle}{\langle \tilde{u}_\phi, u_\phi \rangle + \langle \tilde{v}_\phi, v_\phi \rangle} = 0 \quad (\text{D16})$$

Rotational invariance again implies that the last term on the l.h.s. of Eq. (D16) vanishes (since simply inclining a scroll wave cannot change its rotation frequency) as explicitly shown below (Eq. (D18)). The remaining Eq. (D16) is the equation obtained in ref. [16,12] for the scroll twist dynamics. The coefficient of  $(\partial_z \psi)^2$  simply describes the twist dependence of steady scroll rotation frequency (Eq. (29)) while the coefficient of  $\partial_{zz}^2 \psi$  governs the small  $k_z^2$  dependence of the rotation band [Eq. (23) with the subscript  $t$  replaced by  $\phi$ ].

The computations reported in the present paper permit to explicitly evaluate the four real coefficients which appear in Eq. (D13, D16). For example, for  $a = 0.8, b = 0.01, \epsilon = 0.025$ , the reported results give

$$\frac{\langle \tilde{u}_t, u_t \rangle}{\langle \tilde{u}_t, u_t \rangle + \langle \tilde{v}_t, v_t \rangle} = 0.8842 - 0.662, \quad \frac{\langle \tilde{u}_\phi, u_\phi \rangle}{\langle \tilde{u}_\phi, u_\phi \rangle + \langle \tilde{v}_\phi, v_\phi \rangle} = 0.578, \quad \frac{\langle \tilde{u}_\phi, \partial_{\phi\phi}^2 u_0 \rangle}{\langle \tilde{u}_\phi, u_\phi \rangle + \langle \tilde{v}_\phi, v_\phi \rangle} = -0.7203. \quad (\text{D17})$$

More generally, the two coefficients in Eq. (D16) do not change sign as one traverses the different regions of the phase diagram: a small twist increases the scroll rotation frequency and a small modulation in the  $z$ -direction increases the stability of the rotation band modes. The complex coefficient of Eq. (D13) is directly linked to the scroll wave line tension stability/instability and its real part change sign as 2D spiral drift.

Finally, it may be worth comparing the above derivation to that of [16]. Since the l.h.s of Eq. (D10) is a superposition of terms with different time dependences, this is also the case of its solution and many coefficients formally introduced in ref. [16] do not even appear in our derivation, as previously noted in [12] (in a slightly different formulation). On the other side, we have chosen a simple parameterization for which rotational invariance is not manifest, in contrast to ref. [12]. This forces us to explicitly show that coefficients which do not appear in ref. [12] vanish.

We conclude by showing that indeed,

$$\langle \tilde{u}_\phi, \nabla_{2D}^2 u_0 \rangle = 0. \quad (\text{D18})$$

This is a simple consequence of the transformation property of the reaction-diffusion equations (5, 6) under dilation. Namely,  $(u_0(r(1 + \eta), \phi), v_0(r(1 + \eta), \phi))$  is a solution of (5, 6) with  $\nabla_{2D}^2$  replaced by  $1/(1 + \eta)^2 \nabla_{2D}^2$ . Expanding for  $\eta \ll 1$  gives the infinitesimal version of this transformation

$$\mathcal{L} \begin{pmatrix} r\partial_r u_0 \\ r\partial_r v_0 \end{pmatrix} = 2 \begin{pmatrix} \nabla_{2D}^2 u_0 \\ 0 \end{pmatrix} \quad (\text{D19})$$

which can also be directly checked by differentiating Eq. (5, 6) with respect to  $r$ . The multiplication of Eq. (D19) on both sides by  $(\tilde{u}_\phi, \tilde{v}_\phi)$ , the left eigenvector of  $\mathcal{L}$  of eigenvalue zero, gives the desired identity (D18).

- [1] A.T. Winfree, *When Time Breaks Down* (Princeton U. Press, N. J. 1987).
- [2] V. S. Zykov, *Modelling of wave processes in excitable media* (Manchester U. Press, Manchester, 1988).
- [3] See e.g. the focus issue CHAOS **8**, 1 (1998).
- [4] V. S. Zykov, *Biofizika* **31**, 862 (1986).

- [5] A.T. Winfree, *Chaos* **1**, 303 (1991).
- [6] A. Belmonte, Q. Ouyang and J.M. Flesselles, *J. Phys. II (France)* **7**, 1425 (1997).
- [7] A.T. Winfree, *Science* **266**, 1003 (1994)
- [8] A. M. Pertsov, R. R. Aliev and V. Krinsky, *Nature* **345**, 419 (1990); S. Mironov, M. Vinson, S. Mulvey and A. Pertsov *J. Phys. Chem.* **100**, 1975 (1996).
- [9] A. T. Winfree et al, *Chaos* **6**, 617 (1996).
- [10] C. Henze, E. Lugosi and A. T. Winfree, *Can. J. Phys.* **68** 683 (1989).
- [11] A. V. Panfilov and A. N. Rudenko, *Physica D* **28**, 215 (1987).
- [12] V. N. Biktashev, A. V. Holden and H. Zhang, *Phil. Trans. R. Soc. Lond. A* **347**, 611 (1994).
- [13] Z. Qu, F. Xie, and A. Garfinkel *Phys. Rev. Lett.* **83**, 2668 (1999).
- [14] V. Hakim and A. Karma, *Phys. Rev. E* **60**, 5073 (1999).
- [15] I. Aranson and I. Mitkov, *Phys. Rev. E* **58**, 4556 (1998).
- [16] J.P. Keener, *Physica D* **31**, 269 (1988).
- [17] H. Henry and V. Hakim, *Phys. Rev. Lett.* **85**, 5328 (2000).
- [18] R. FitzHugh, *Biophys. J.* **1**, 445 (1961); J. Nagumo, S. Arimoto and S. Yoshizawa, *Proc. I. R. E.* **50**, 2061 (1962).
- [19] D. Barkley, *Physica D* **49**, 61 (1991)
- [20] I. Goldhirsch, S. A. Orszag and B. K. Maulik, *J. Scient. Comp.* **2**, 33 (1987).
- [21] D. Barkley, *Phys. Rev. Lett.* **68**, 2090 (1992); *Phys. Rev. Lett.* **72**, 164 (1994)
- [22] Other dangerous modes and instabilities (like alternans see e.g. A. Karma, *Proc. Nat. Acad. Sci. USA* **97**, 5687 (2000)). can arise in more complicated cases. We do not consider them here.
- [23] I. Mitkov, I. Aranson and D. A. Kessler, *Phys. Rev. E* **52**, 5974 (1995).
- [24] S. Fauve p. 446 in *Hydrodynamics and nonlinear instabilities*, C. Godrèche and P. Manneville editors (Cambridge U. Press, Cambridge, U.K., 1998)
- [25] V. Krinsky, E. Hamm and V. Voignier, *Phys. Rev. Lett.* **76**, 3854 (1996).
- [26] L. Landau and E. Lifchitz *Théorie de l'élasticité* (Mir, Moscou, 1990); A. E. H. Love, *A Treatise on the Mathematical Theory of Elasticity* (Cambridge U. Press, Cambridge, 1952) and references therein.
- [27] I. S. Aranson and A. R. Bishop *Phys. Rev. E* **57**, 5276 (1998); M. Gabbay, E. Ott, and P. Guzdar, *Physica (Amsterdam)* **118D**, 371 (1998); G. Rousseau, H. Chaté, and R. Kapral, *Phys. Rev. Lett.* **80**, 5671 (1998).
- [28] D. Margerit and D. Barkley, *Phys. Rev. Lett.* **86**, 175 (2001).
- [29] V. Hakim, H. Henry and A. Karma (unpublished).
- [30] A. V. Panfilov and J. P. Keener, *Physica D* **84**, 545 (1995).
- [31] F. Fenton and A. Karma, *Phys. Rev. Lett.* **81**, 481 (1998); *Chaos* **8**, 20 (1998).
- [32] W.-J. Rappel *Chaos* **11**, 71 (2001).
- [33] S. Setayeshgar and A. Bernoff, *Phys. Rev. Lett.*, (in press).
- [34] W. T. Baxter et al, *Biophys. J.* **80** 516 (2001).
- [35] W.H. Press et al, pp 63-82 in *Numerical Recipes in Fortran* (Cambridge University Press, U.K. 1992).
- [36] M. Dowle, R.M. Mantel and D. Barkley, *Int. J. Bif. Chaos* **7**, 2529 (1997).
- [37] K.I. Agladze and P. de Kepper, *J. Phys. Chem.* **96**, 5239 (1992).
- [38] O. Steinbock, J. Schütze and S.C. Müller, *Phys. Rev. Lett.* **68**, 248 (1992).
- [39] A. Belmonte and J.M. Flesselles, *Europhys. Lett.* **32**, 267 (1995).
- [40] J.H. White, *Amer. J. of Math.* **91**, 693 (1969); W. F. Pohl, *Math. Intell.* **3**, 20 (1980) and references therein.
- [41] F.B. Fuller, *P.N.A.S.* **75**, 3557-3561 (1978).

